Characterization of the Magnetic Particle Imaging Signal Based on Theory, Simulation, and Experiment

by Jan-Philip Gehrcke

A thesis submitted in partial fulfillment
of the requirements for the degree
Master of Science with Honors
in Physics

supervised by
Prof. Dr. Peter M. Jakob and **Dr. Volker C. Behr**
University of Würzburg, Experimental Physics 5

2010

Abstract

Magnetic Particle Imaging (MPI) is a novel imaging modality allowing for the detection of the spatial distribution of magnetic nanoparticles at high spatio-temporal resolution. This thesis provides a comprehensive theoretical part, describing the origin and the properties of the signal in MPI as well as the most important dependencies.

The impact of magnetic particle interaction on the MPI signal is investigated by simulation and experiment: it is shown that higher harmonic amplitudes A_n are not linearly related to particle concentration c, as misleadingly suggested by LANGEVIN's single particle model (SPM). Therefore, current linear image reconstruction schemes have to be revised. A more sophisticated magnetization theory matches experimentally gained $A_n(c)$ data very well and consequently is the preferable choice over the SPM.

Finally, this thesis presents a new method for the detection of magnetic particle agglomerates/clusters based on the nonlinear $A_n(c)$ relation. This method can be applied to test for specific substances or processes on a molecular level.

Meinen Eltern

Contents

Chapter 1

Introduction

In 2005, Magnetic Particle Imaging (MPI) has been introduced as an imaging technique to perform background-free detection of the spatial distribution of magnetic nanoparticles (made of e.g. iron oxide) in biological tissue [1]. In particular, regarding cellular and molecular imaging or e.g. angiography, MPI may surpass contrast agent-based Magnetic Resonance Imaging (MRI), due to the intrinsic features of the method: *high sensitivity* and – concurrently – *high temporal resolution*. Therefore, MPI is a research and diagnostic platform with high potential.

In MPI, the detection of magnetic nanoparticles is based on their non-linear magnetization response. Due to the design of the method,

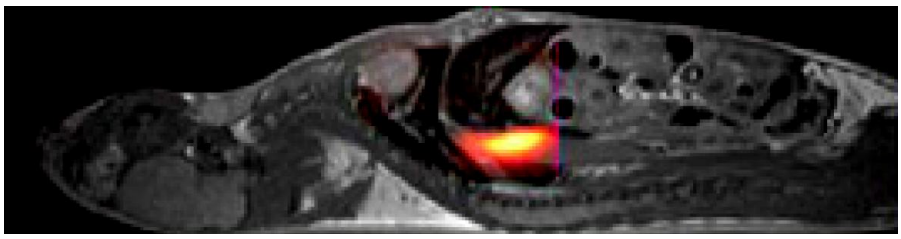

Figure 1.1: Picture taken out of [2]. Three-dimensional MPI angiography of a mouse, after injecting a magnetic tracer into its tail vein. **Color**: MPI image, taken out of a time series of three-dimensional datasets. The tracer bolus just goes through *vena cava*. **Gray**: Corresponding anatomy image of the same mouse, done in a separate MRI.

these particles are detected with *positive* contrast. In a biological system, everything surrounding the particles has a linear magnetization response, ideally leading to no false-positive MPI background signal in medical applications. This is a huge advantage over MRI. Here, magnetic nanoparticles destroy signal, leading to a *negative* contrast. Therefore, MPI has the potential to be more conclusive than contrast agent-based MRI.

The first serious MPI results have been presented in 2009 [2]: the authors managed to accomplish a three-dimensional real-time angiography of a mouse, as indicated in Figure 1.1. However, the theory MPI is built on still is in the process of establishment and has to be investigated. This is where this thesis starts.

Based on important physical concepts like superparamagnetism, magnetic particle spectroscopy and non-linear response in general, the investigations in this work concentrate on the impact of particle concentration c on the MPI signal. This is very important, since for tomography, the spatial particle distribution $c(\vec{x})$ has to be reconstructed from the MPI signal. To gain a quantitatively correct image, the dependency of the MPI signal on c has to be known exactly and accounted for. At this point, previous works used a very simple magnetization theory, LANGEVIN's single particle model, which yields a linear relation between signal an c.

However, due to magnetic dipole-dipole interaction, this actually is a non-linear relation. In this work, the concept of MPI is extended by investigating the impact of magnetic particle interaction theoretically, by simulation, and by experiment.

Chapter 2

MPI basics

This chapter is a detailed composition of MPI's fundamental theory. The primary goal is to prepare the special approaches and deliberations of this thesis. Another intention of this chapter is to form an *entire* MPI starter reference, providing theoretical background for all important concepts MPI is constituted of.

2.1 Overview

A *ferrofluid* is a suspension of magnetic nanoparticles[1]. If each particle features a *giant magnetic moment*, the fluid behaves *superparamagnetic*, resulting in a strong magnetization response to externally applied magnetic fields. This phenomenon of superparamagnetism will be described in part 2.3.

The interaction of a ferrofluid with an external magnetic field – and, in particular, its magnetization response to it – is the essence of most applications incorporating ferrofluids. Likewise, MPI is built on top of this magnetization response. Fundamental research in MPI starts with the understanding of and the ability to predict a ferrofluid's magnetization behavior. Therefore, after a general description of ferrofluids in part 2.4, the simplest case to consider theoretically, a dilute[2] ferrofluid,

[1] Particles with dimensions on nanometer scale.

[2] A ferrofluid with very low particle concentration.

will be discussed in part 2.4.3, introducing LANGEVIN's *single particle model*.

With this theoretical background, the reader is well-prepared to get confronted with "zero-dimensional MPI": the spectroscopical evaluation of a ferrofluid's *non-linear magnetization response*, which is described in part 2.5.

Finally, GLEICH and WEIZENECKER's methods for determining the spatial distribution of magnetic particles are explained in part 2.6.

2.2 Paramagnetism

A system of noninteracting atomic magnetic moments obeys the laws of ideal CURIE paramagnetism [3]. Such a system's relative magnetization in an external magnetic field is derived now, using a mixture of quantum mechanics and classical statistics.

Consider a single magnetic moment $\vec{m}$ with quantum mechanical behavior[1]:

$$\vec{m} = g\mu_B \frac{\vec{J}}{\hbar}, \tag{2.1}$$

where g is the LANDÉ factor, μ_B is BOHR's magneton, $\hbar$ is the reduced PLANCK constant, and $\vec{J}$ is the total quantum mechanical angular momentum (the sum of spin and orbital contributions). Let J be the corresponding total angular momentum quantum number.

Consider a z-direction, defined by an external magnetic field $\vec{B}$ ($|\vec{B}| = B_z \equiv B$). The projection of $\vec{J}$ on the z-axis is $\vec{J_z}$; its absolute value is J_z and the corresponding quantum number is j_z:

$$J_z = \hbar j_z \tag{2.2}$$

A quantum mechanical system with total angular momentum number J has exactly $2J+1$ discrete states, distinguished by $j_z = -J, -J+1, \ldots, J-1, J$. The quantized J_z is leading to a quantized z-component of the magnetic moment m_z:

$$m_z(j_z) = g\mu_B \frac{J_z}{\hbar} = g\mu_B j_z \tag{2.3}$$

[1] E.g. a single atom.

The magnetic moment's absolute potential energy is $m_z(j_z) \cdot B$, so the system's energy splits up into discrete levels for $B \neq 0$ (ZEEMANN splitting).

Having these energetically discrete system states, the mean magnetic moment $\langle m_z \rangle$ in field direction for a given temperature T is easy to derive from classical BOLTZMANN statistics[1]:

$$\langle m_z \rangle = g\mu_B \langle j_z \rangle = \frac{g\mu_B}{Z} \sum_{j_z=-J}^{j_z=+J} j_z \mathrm{e}^{-\frac{m_z(j_z)B}{kT}} \tag{2.4}$$

with the partition function

$$Z = \sum_{j_z=-J}^{j_z=+J} \mathrm{e}^{-\frac{m_z(j_z)B}{kT}}. \tag{2.5}$$

and the BOLTZMANN constant k.

Considerable manipulation of Equation (2.4) leads to the quantum mechanical BRILLOUIN function $\mathcal{B}_J(B,T)$, giving a directly evaluatable expression for $\langle m_z \rangle$ [4]:

$$\langle m_z \rangle = g\mu_B J \mathcal{B}_J(B,T) \tag{2.6}$$

with

$$\mathcal{B}_J(B,T) = \frac{2J+1}{2J} \coth\left(\frac{2J+1}{2J}a\right) - \frac{1}{2J}\coth\left(\frac{a}{2J}\right), \tag{2.7}$$

whereas

$$a = \frac{g\mu_B JB}{kT}. \tag{2.8}$$

Paramagnetic system's magnetization behavior

Now consider a system made of many noninteracting quantum mechanical magnetic moments. $\mathcal{B}_J(B,T)$ provides the whole system's relative magnetization M_{rel}:

$$M_{rel} = \frac{\langle M_z \rangle}{M_\infty} = \mathcal{B}_J(B,T). \tag{2.9}$$

[1] Here, minimization of magnetic energy is the opponent of thermal agitation.

$\langle M_z \rangle$ is the mean total magnetization in field direction. M_∞ is the theoretical saturation magnetization for $B \to \infty$. Saturation is reached, if all magnetic moments had maximum allowed[1] alignment with the external magnetic field.

In the absence of an applied field, the independent atomic moments – driven by thermal energy – point at random directions and cancel out each other. Thus, in this case, the system's total magnetization is zero. This is characteristic for paramagnetic systems.

2.3 Superparamagnetism

Magnetostatic energy in a ferro- or ferrimagnet is minimized by forming the material into magnetic domains. But formation of domains costs energy itself and so there is a critical minimum domain size that minimizes the total energy of the system. Consequently, a single particle of a size below the minimal domain size is a homogeneously magnetized single-domain particle [5].

2.3.1 Classical limit: giant magnetic moments

A single-domain particle may consist of 10^4 or even many more single atoms [4]. Below the CURIE temperature, this means that all these atomic magnetic moments in this single magnetic domain are strongly coupled and yield a giant total magnetic moment [5]. The critical particle size, up to which the single-domain state is the energetically preferred one, depends on the actual material and is on the order of 1 to $100\,\mathrm{nm}$. Detailed numbers regarding different materials are delivered in [6].

The magnetization of a system constituted by noninteracting giant magnetic moments can be perfectly described by the theory of CURIE's paramagnetism, as introduced in part 2.2. It is just the size of the magnetic moment and the angular momentum quantum number J that have to be chosen properly.

When magnetic moment carriers involve so many elementary magnetic moments as single-domain particles do, quantum effects get ir-

[1] For quantum mechanical magnetic moments, the z-component is limited as given by Equation 2.3. Thus, completely parallel alignment is not allowed.

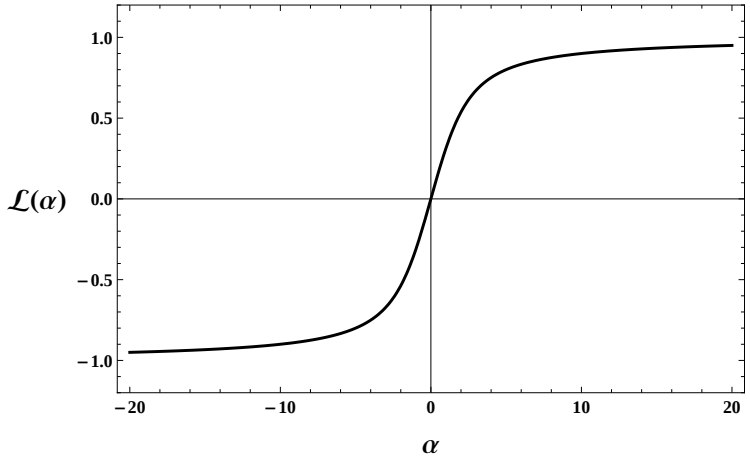

Figure 2.1: Classical limit of the BRILLOUIN function, the LANGEVIN function $\mathcal{L}(\alpha)$. It is used to calculate the relative magnetization of a system of noninteracting and freely rotatable magnetic moments.

relevant. This is due to an extremely high spin quantum number J, allowing virtually free alignment of the giant magnetic moment to an externally applied field. Then, it is justified to consider the classical limit of CURIE's paramagnetism, which is represented by the BRILLOUIN function $\mathcal{B}_J(B,T)$ evaluated for $J \to \infty$ [7] at room temperature:

$$\mathcal{B}_\infty(B,T) = \mathcal{L}\left(\frac{mB}{kT}\right) \tag{2.10}$$

where $m \equiv |\vec{m}|$ is the giant magnetic moment and $\mathcal{L}(\alpha)$ the LANGEVIN function:

$$\mathcal{L}(\alpha) = \coth(\alpha) - \frac{1}{\alpha} \tag{2.11}$$

Hence, applying a magnetic field to a system of noninteracting and freely rotatable giant magnetic moments will induce a relative magnetization as given by $\mathcal{L}(\alpha)$ (see Figure 2.1).

2.3.2 Néel and Brown relaxation processes

The classical limit of CURIE's paramagnetism, when single magnetic moments can be considered as classic magnetic dipoles, is commonly

called *superparamagnetism*. Particles on the nanometer scale, exhibiting giant magnetic moments, are commonly called *superparamagnetic* particles, with "super" meaning large, as in superconductivity.

But this is not the entire definition of superparamagnetism. Two different relaxation mechanisms have to be distinguished to define it correctly. The consideration of both relaxation types, NÉEL and BROWN relaxation, is very important for applications of superparamagnetic nanoparticles, like MPI.

Néel relaxation

The original meaning of superparamagnetism described a phenomenon pointed out by NÉEL. Consider a *mechanically fixed* single-domain particle. All its elementary quantum mechanical angular momentums are coupled. The resulting giant magnetic moment is rigidly bound by one or more of the possible anisotropies within the crystalline material the particle is made of. It is "frozen" within the particle. For big particles, the anisotropical energy E_{AI} of this bond is very high in comparison with realistic magnetic or thermal energies. But it changes quickly with the particle's volume. While shrinking this, a critical barrier is passed. Below, the thermal energy kT is strong enough to disrupt the magnetic moment's bonding to the particle itself [5].

The NÉEL relaxation time $\tau_N(E_{AI}/kT)$ is a gauge for the mobility of a giant magnetic moment within a mechanically fixed particle. Considerably below the critical particle size, the magnetic moment is free to move and respond to an applied field, resulting in τ_N to of order 10^{-9} s. Around the critical particle size, τ_N changes by the factor 10^9 for a volume variation of the factor 2 [8].

Considering a fixed particle with a size below the critical one, an externally applied magnetic field would try to align the giant magnetic moment, fighting against kT. This is the classical limit of CURIE's paramagnetism. Hence, the relative magnetization is accurately described by the LANGEVIN theory.

Brown relaxation

In the framework of most applications, magnetic single-domain particles are suspended in a liquid. In these cases, they are able to rotate

mechanically, subjected by BROWNIAN movement. Since the counter-force against such rotation is of hydrodynamic origin, the corresponding BROWN relaxation time τ_B depends on thermal energy, particle volume and the liquid carrier's viscosity. For water or kerosene as solvent, τ_B is on the order of 10^{-7} s [8].

2.3.3 Critical sizes and characteristical time scales

There are two critical particle volumes. First, V_{sd}, below which the single-domain state is energetically preferred, exhibiting a giant magnetic moment. Second, an even smaller volume, V_{sp}, below which this giant magnetic moment is able to rotate almost freely within the mechanically fixed particle, governed by the NÉEL relaxation time τ_N and showing superparamagnetism in its original sense.

Particles with a volume below V_{sd} but above V_{sp} are important for all applications that require single-domain nanoparticles with huge magnetic moments. But they cannot automatically be considered as *superparamagnetic* (i.e, in the sense of the phenomenon NÉEL discovered and describable with the LANGEVIN theory). Both of the following conditions must be fulfilled:

- The particles have to be able to rotate mechanically (as is the case when they are solved in a liquid carrier).
- Magnetic field changes and measurements must happen on a larger time scale than given by τ_B.

Then, it is fundamentally the same as "NÉEL's superparamagnetism": an external field would fight thermal energy and try to align the magnetic moment by – this time – *mechanical rotation of the whole particle*. From this it follows that such a system is described correctly by the LANGEVIN theory, too. The case described can be considered as "BROWN's superparamagnetism".

As stated in [5], the critical particle diameter for iron, below which "real" superparamagnetism in the sense of NÉEL occurs, is $8.5\,\mathrm{nm}$. Below that size, the dominant relaxation mechanism is the NÉEL relaxation, even for mechanically rotatable particles. This type of relaxation ($\tau_N \approx 10^{-9}$ s) is allowing higher excitation and measuring rates than

for bigger particles, which are dominated by mechanical and slower BROWN relaxation ($\tau_B \approx 10^{-7}$ s).

These time scales are important to consider in MPI, e.g. for choosing an appropriate excitation frequency.

2.3.4 Para- vs. superparamagnetism

The fundamental behavior of paramagnetic and superparamagnetic systems is the same, regarding the fact that thermal energy works against the alignment of independent magnetic moments with an applied magnetic field: there is no hysteresis and no residual field. But there are two crucial differences between para- and superparamagnetism: *the field-dependency of the magnetic susceptibility* χ and *the absolute magnetization values for the same external field strength*.

The magnetic susceptibility χ is defined as the change of magnetization M with the magnetic field H:

$$\chi = \frac{\partial M}{\partial H}, \tag{2.12}$$

where $H = B/\mu$ and μ is the magnetic permeability.

While CURIE paramagnetism is stronger than e.g. diagmagnetism, it's still weak in comparison with magnetically ordered states (like e.g. ferromagnetism). At room temperature, typical magnetic susceptibilities of substances showing CURIE paramagnetism are not higher than 10^{-2} [3].

Each superparamagnetic particle behaves like a huge atom, with its angular momentum quantum number J_{SP} being by a factor of several orders of magnitude higher than J_P of a conventional paramagnet. This factor is the same between the resulting magnetic moments m. The argument of the BRILLOUIN and LANGEVIN function is proportional to the magnetic energy mB. Hence, the factor of several orders of magnitude between J_{SP} and J_P arises again for the resulting magnetic susceptibilities and absolute magnetization values, considering the linear regime of the BRILLOUIN and LANGEVIN functions.

In case of CURIE paramagnetism, it's actually "impossible" to leave the linear regime: for room temperature, saturation cannot be achieved with the most powerful magnets [4]. Hence, the magnetic

susceptibility χ is field independent: **paramagnetic magnetization behavior is always linear**.

Superparamagnetic systems can easily be saturated, with moderate magnetic field strengths, generable by conventional magnets. The initial susceptibility χ_{init} (around zero magnetic field) is much higher than typical magnetic susceptibilities of substances showing CURIE paramagnetism. Here, the discussed factor of several orders of magnitude appears again. χ decreases for bigger field strengths. In the regime of saturation, it converges to zero. Hence, **superparamagnetic systems (more general, systems made of giant magnetic moments) can easily be provoked to display non-linear magnetization behavior**.

2.4 Ferrofluids

2.4.1 General properties

Ferrofluids (also called ferrocolloids or magnetic fluids) are colloidal fluids, constituted of magnetic particles, which are most often made of or containing ferro- or ferrimagnetic material. The particles are suspended in a carrier fluid, which usually is an organic solvent, like kerosene or water.

Ferrofluids are stabilized with the help of special surfactants the magnetic particle cores are coated with. This prevents local agglomeration[1] due to magnetic and VAN-DER-WAALS forces as well as decomposition of the magnetic cores, leading to highly persistent suspensions.

A true ferrofluid does not settle out and therefore is made of nanoparticles [9]. Then, thermal energy is sufficient to overcome gravitational effects: BROWNIAN motion keeps the particles homogeneously suspended.

If the particles are noninteracting (far away from each other) and exhibit a giant magnetic moment (like homogeneously magnetized single-domain particles), the whole fluid shows superparamagnetic magnetization behavior and is called a *superparamagnetic ferrofluid*.

The liquid carrier allows the particles to rotate mechanically. Depending on the actual size of the particles within the fluid, either the

[1] Or “aggregation”: sticking together of particles.

NÉEL or the BROWN form of superparamagnetic relaxation is dominating the ferrofluid's response to externally applied magnetic fields, as explained in part 2.3.3.

Particle diameters and magnetic moments

The most widely used ferrofluids are based on spherically shaped nanoparticles, i.e. the cores made of magnetic material are assumed to be spheres. Surface effects lead to spin disordering, so the core is surrounded by a demagnetized layer [10]. The effective magnetic core diameter d only describes the homogeneously magnetized inner sphere. This inner part of the particle can be considered as bulk material like in a large-scale solid state. Hence, the bulk saturation magnetization M_s of the corresponding material is valid for the homogeneously magnetized inner sphere, too.

To be able to make a clear statement about the magnetizability of a superparamagnetic ferrofluid, it is essential to know the actual strength of the giant magnetic moments m the ferrofluid is constituted of. Since magnetization M is magnetic moment m per volume V, the general relation

$$m = MV \tag{2.13}$$

can be used to calculate the magnetic moment of a spherically shaped particle in dependence of its magnetic core diameter d:

$$m(d) = \frac{\pi}{6} M_s d^3 \tag{2.14}$$

During the synthesis of superparamagnetic nanoparticles (different techniques are listed in e.g. [11]), a whole distribution of magnetic core diameters is created. Depending on the actual production method and some size selecting postprocessing (which can be done by filtration and centrifugation), a more or less wide diameter distribution can be found in the resulting ferrofluid.

For an entire description of a particular ferrofluid sample, it is necessary to know the magnetic core diameter probability distribution function $p(d)$, which can be used to e.g. calculate the mean magnetic moment $\langle m(d) \rangle$:

$$\langle m(d) \rangle = \int_0^\infty p(d) m(d) \, \mathrm{d}d \ . \tag{2.15}$$

Measuring $p(d)$ is a non-trivial task, as will be described in part 3.1; but exact awareness is of particular importance: it excludes a huge uncertainty in experiments and enables to reproduce experimental results in simulations.

Ferrofluids with an *extremely* sharp distribution $p(d)$ are considered as *monodisperse*, while all other ferrofluids are called *polydisperse*, i.e. they consist of particles with significantly different magnetic core diameters.

2.4.2 Ferrofluids as contrast agents

In nuclear magnetic resonance imaging (MRI), superparamagnetic nanoparticles are well-established as contrast agents for molecular imaging, i.e. gathering both anatomic and information on the molecular level simultaneously: the giant magnetic moments are strong spin-spin relaxation enhancers and therefore destroy nuclear magnetic resonance signal in their vicinity. In MPI, basically the same contrast agents can be utilized to determine their spatial distribution.

Due to their nontoxicity, superparamagnetic iron-oxide nanoparticles (SPIOs) are well-suited for medical applications in organisms like humans [11]. Typically, the iron-oxide particle cores are enveloped in a polysaccharide or synthetic polymer coating. A popular exterior coating material is *dextran* or *citrate*, whereas the magnetic core is often made of ferrimagnetic *magnetite* (Fe_3O_4) or *maghemite* (γFe_2O_3). Depending on the actual particle size, shell structure and functionality, there are many SPIO subclasses, like USPIO, MION, VSOP, CLIO and others. A detailed description of these particle classes can be found in [11], [12], and [13]. Furthermore, detailed listings of commercial SPIO agents are shown, including their state of clinical approval.

For medical applications, the coating can be used to ensure biocompatibility if the core itself is toxic, as is the case for cobalt, which exhibits a much higher magnetic moment per particle volume (bulk saturation magnetization M_s) than e.g. magnetite. Cobalt nanoparticles can be rendered nontoxic, if they are coated with gold [14] or citrate [15].

If noninteracting giant magnetic moments are – as contrast agent – injected into a biological system in form of stable particles, *the whole*

system can be considered as superparamagnetic ferrofluid, regardless of the particle's particular realization.

2.4.3 Single Particle Model: dilute ferrofluids' magnetization theory

The ferrofluid's magnetization curve $M(H)$ is the key quantity to calculate the magnetization response to an externally applied or irradiated magnetic field, if all other parameters are known.

In this part, the magnetization curve of a ferrofluid is discussed in terms of LANGEVIN's theory of superparamagnetism, i.e. noninteracting giant magnetic moments are assumed, as it is well-established in MPI literature, e.g. in [16]. This ferrofluid magnetization model will henceforth referred to as **S**ingle **P**article **M**odel (**SPM**).

Consider a polydisperse ferrofluid constituted of particles yielding an effective magnetic material density $\rho \in]0, 1]$, whereas the maximum density $\rho = 1$ corresponds to the bulk material. The goal is to calculate the system's total magnetization $M_{SPM}(H, \rho)$ in terms of the SPM, consulting the Equations 2.10 and 2.11, which describe the relative magnetization of a superparamagnetic system. Using the magnetic core diameter probability distribution function $p(d)$ for averaging, this results in the relative magnetization

$$M_{rel,SPM}(H) = \left\langle \mathcal{L}\left(\frac{\mu_0 m(d) H}{kT}\right)\right\rangle . \tag{2.16}$$

μ_0 is the vacuum permeability and kT the thermal energy. With a specific system's saturation magnetization M_∞ (for $H \to \infty$), the total magnetization is generally given by

$$M(H) = M_\infty M_{rel}(H) \tag{2.17}$$

(cf. Equation 2.9). Considering ρ as the *global* density, defining the magnetic phase volume fraction of the sample's total volume, yields $M_\infty = \rho M_s$, with M_s being the bulk saturation magnetization of the magnetic material. Hence, the SPM's total magnetization can be expressed as

$$M_{SPM}(H, \rho) = \rho M_s \left\langle \mathcal{L}\left(\frac{\mu_0 m(d) H}{kT}\right)\right\rangle . \tag{2.18}$$

Strictly seen, the SPM is valid only in the limit $\rho \to 0$, because LANGEVIN's theory of superparamagnetism assumes *noninteracting* magnetic moments, which requires infinite distances between them. In reality, the SPM predicts proper ferrofluid magnetization values if the single giant magnetic moments *almost* do not "see each other". This is the case for very *dilute* fluids, when the interparticle magnetic coupling energy (due to dipole-dipole exchange interaction) is very small in comparison with the energy of a single moment in the externally applied field.

Neglecting interparticle interactions results in a model that is linear in ρ (Equation 2.18 yields $M_{SPM}(H, \rho) \propto \rho$). Obtaining a theoretical model that is valid for moderate and high particle densities, requires the incorporation of magnetic interparticle coupling, which then leads to a non-linear magnetization dependency on ρ, as will be discussed in part 3.2.

2.5 Magnetic Particle Spectroscopy

Consider a system containing magnetic particles, getting excited by a harmonically oscillating magnetic field. The system then sends out another magnetic field; its *magnetization response*. If the system's magnetic susceptibility χ is *not* constant within the range of the excitation field strength, the magnetization is non-linearly dependent on the externally applied field strength. As explained in part 2.3.4, for systems made of giant magnetic moments, χ already varies for relatively small excitation field strengths.

In case of varying χ, the considered magnetic system features *non-linear response*, a phenomenon that is generally known from various physical systems exhibiting non-linear effects. A non-linear magnetization response contains integer multiples of the harmonically irradiated magnetic field's frequency, so-called *higher harmonics*. The higher harmonics' general origin will be explained mathematically in part 2.5.1, introducing non-linear response theory. Higher harmonics in a ferrofluid's magnetization response will be analyzed separately in part 2.5.2.

A ferrofluid's magnetization response can be detected inductively and evaluated spectroscopically. Such an experiment could be con-

sidered as "zero-dimensional MPI", but a more appropriate term may be **M**agnetic **P**article **S**pectroscopy (**MPS**). MPS can be used to e.g. investigate the characteristics of MPI contrast agents or for fundamental research regarding the magnetization behavior of ferrofluids.

2.5.1 Nonlinear response theory

Many simple physical systems behave linear. There, e.g. displacements or accelerations are linear to forces and currents are linearly related to voltages, etc. Consider a system with an output quantity f that is the *response* to some input x. $f(x)$ is the transfer function between input and output, characterizing the response behavior of the system.

Linear systems satisfy

$$f_{lin}(x) = K \cdot x + C, \tag{2.19}$$

where K and C are constants. But, there also are many physical systems obeying non-linear laws due to *non-linear effects*, which are of practical importance in various fields of physics. The following example should help to understand a crucial consequence of non-linear response: the *generation of higher harmonics* by a harmonically excited non-linear responding system.

Harmonical excitation of a third-order non-linear system

Consider a non-linear distortion of a linear system[1], which is a third-order distortion in this case:

$$f_{nonlin}(x) = K \cdot (x + \epsilon x^3) \tag{2.20}$$

ϵ defines the distortion's relative strength. $f_{nonlin}(x)$ is compared to $f_{lin}(x)$ in Figure 2.2. Now suppose a *harmonically* oscillating excitation of the system, i.e. the input exactly follows a sine or cosine curve over the time t:

$$x_{harmonic}(t) = A_0 + A\sin(\omega t + \phi) \tag{2.21}$$

[1] To simplify matters, the offset C of Equation 2.19 is set to 0.

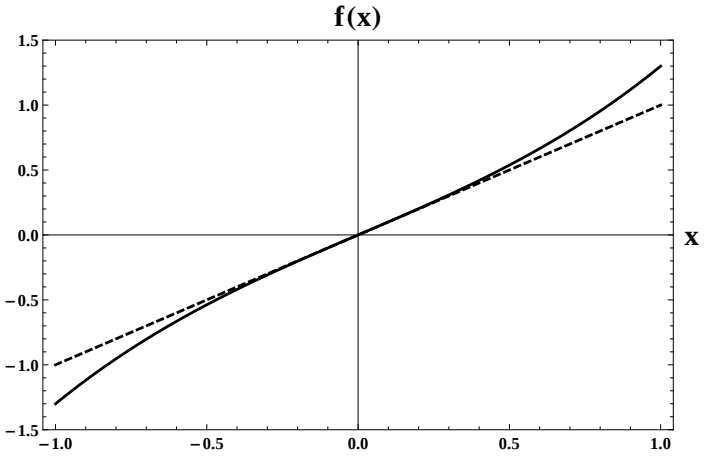

Figure 2.2: A physical system's transfer function $f(x)$: response/output f in dependence of the excitation/input x. Solid line: predominantly linear responding system with small third-order non-linearity (Equation 2.20 with $\epsilon = 0.3, K = 1$). Dashed line: linear responding system ($K = 1$).

At this point, the simplest harmonic trajectory is treated, with $A_0 = 0$, $A = 1$, $\phi = 0$ and the excitation frequency $\omega = \omega_0$:

$$x(t) = \sin(\omega_0 t) \tag{2.22}$$

The response then is

$$f_{nonlin}(t) = K \cdot \left(\sin(\omega_0 t) + \epsilon \sin^3(\omega_0 t)\right). \tag{2.23}$$

Using

$$\sin^3(y) = \frac{1}{4}\left(3\sin(y) - \sin(3y)\right) \tag{2.24}$$

to replace $\sin^3(\omega_0 t)$ with power-free harmonical terms yields

$$f_{nonlin}(t) = \left(K + \frac{3K\epsilon}{4}\right)\sin(\omega_0 t) - \frac{K\epsilon}{4}\sin(3\omega_0 t). \tag{2.25}$$

The response of a system with linear transfer function would have been

$$f_{lin}(t) = K \cdot \sin(\omega_0 t), \tag{2.26}$$

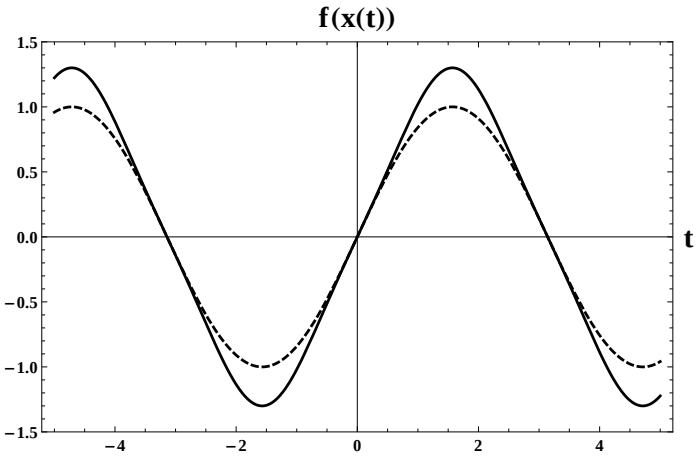

Figure 2.3: Harmonically excited system's response $f(x(t))$. Solid line: predominantly linear responding system with third-order non-linearity (Equations 2.22 and 2.23 with $\epsilon = 0.3, K = 1, \omega_0 = 1$). Dashed line: linear responding system ($K = 1$).

i.e. harmonically oscillating with the excitation frequency ω_0 and altered amplitude. In contrast, the third-order non-linearity in the transfer function has caused significant changes in the system's response. As it is obvious from Equation 2.25, the amplitude of the fundamental (excitation) part changes, too and – in particular – *a harmonic contribution with frequency* $3\omega_0$ *appears* (proportional to ϵ). This is a so-called *higher harmonic* of the fundamental frequency ω_0 and since it is the triple fold, it is the *third harmonic*. In Figure 2.3 both, the linear and non-linear systems' responses to harmonical excitation are compared.

As a result of non-linear response, the overall response signal is distorted: it has contributions of *different frequencies* and, hence, it is no more harmonic.

Generation of higher harmonics: a general consideration

An arbitrarily shaped periodic function or signal with periodicity $T = 2\pi/\omega_0$ is a linear combination of the *fundamental harmonic* part with frequency ω_0 and – depending on the actual signal shape – a number of higher harmonic contributions, whose frequencies are integer multiples of ω_0. Contributions with other frequencies will not be found, no matter

what the actual signal's shape is. This is plausible, since any frequency contribution ω that does not fulfill $\omega = n\omega_0$ with $n \in \mathbb{Z}$ has no mutual periodicity with $2\pi/\omega_0$. Hence, something else than $n\omega_0$-contributions would destroy the signal's overall T-periodicity, implying the fact that any arbitrarily shaped periodic signal must be constituted of single harmonic contributions fulfilling $\omega = n\omega_0$.

This was the intuitive and vivid version of a coherence, that, of course, can also be described more entirely and formally: a periodic function $p(t)$ with the fundamental frequency $\omega_0 = 2\pi/T$ can be represented as a FOURIER series:

$$\begin{aligned} p(t) &= p(t+T) \\ &= \sum_{n=0}^{\infty} a_n \cos(n\omega_0 t) + b_n \sin(n\omega_0 t) \qquad (2.27) \\ &= \sum_{n=-\infty}^{\infty} c_n \mathrm{e}^{in\omega_0 t} \qquad (2.28) \end{aligned}$$

Hence, $p(t)$ is a linear combination of only harmonical functions (sine, cosine) with different frequencies $n\omega_0$ ($n \in \mathbb{Z}$) and distinct amplitudes (a_n, $b_n \in \mathbb{R}$). In the course of a FOURIER analysis, the periodic signal $p(t)$ is decomposed in its harmonical constituents, yielding the amplitudes a_n and b_n or $c_n \in \mathbb{C}$. These coefficients can be used to calculate the power spectral density $P(\omega)$ (also simply called the *spectrum*) of the periodic signal $p(t)$. As argued, this ideally is a discrete spectrum with $P(\omega) \neq 0$ only for $\omega = n\omega_0$.

Think of a system with an *arbitrarily* shaped transfer function $f(x)$, driven/excited periodically by an *arbitrarily* shaped input $x(t)$, with only one, but very important, constraint: $x(t)$ must feature T-periodicity. Independent of the actual forms of $f(x)$ and $x(t)$, the response $f(x(t))$ then is T-periodic, too:

$$f(x(t)) = f(x(t+T)) \qquad (2.29)$$

In this particular case, Equation 2.27 implies that **the response signal of a periodically driven system is *always only* composed of discrete harmonical contributions fulfilling $\omega = n\omega_0$, no matter if the excitation itself is harmonical or not.**

Considering *harmonical* input $x(t)$ (as given by 2.22), it is possible to predict the response's higher harmonic contributions in dependence

of the actual transfer function $f(x)$. In the example above, it was shown that a third-order non-linearity leads to a $3\omega_0$ contribution. Calculating with a second-order non-linearity leads to a $2\omega_0$ term, due to

$$\sin^2(y) = \frac{1}{2}(1 - \cos(2y)), \tag{2.30}$$

providing a reason to believe that there is a strict connection. The intention of the next paragraphs is to enlighten this for the n-th order non-linearity.

A transfer function's non-linearity of n-th power results in a $\sin^n(y)$ term in the response (in case of $x(t) = \sin(\omega_0 t)$). In order to understand the harmonical contributions introduced by an n-th power non-linearity, the decomposition of $\sin^n(y)$ into a sum of power-free sines or cosines, as it was done in Equations 2.24 and 2.30 for $n = 2,\ 3$, is helpful. The general decomposition rule for $n \in \mathbb{Z}$ is derived in [17]. The result is presented here; even and odd ns must be treated separately:

for **odd** n :

$$\sin^n(y) = \frac{(-1)^{(n-1)/2}}{2^n} \sum_{k=0}^{n} (-1)^k \binom{n}{k} \sin((n-2k)y) \tag{2.31}$$

for **even** n :

$$\sin^n(y) = \frac{(-1)^{n/2}}{2^n} \sum_{k=0}^{n} (-1)^k \binom{n}{k} \cos((n-2k)y) \tag{2.32}$$

$2k$ always is an even number. Subtracting an even number from an odd-/even number results in an odd/even number, correspondingly. Hence, the formulas above show that if n is *odd*, $\sin^n(\omega_0 t)$ is decomposable into a linear combination of sines with *only odd* multiples of the fundamental frequency ω_0, up to $n\omega_0$ (for $k = 0$). If n is *even*, $\sin^n(\omega_0 t)$ is decomposable into a sum of cosines with *only even* multiples of the fundamental frequency ω_0. Here, the highest appearing frequency is $n\omega_0$, too. So the harmonical contributions introduced by an n-th power non-linearity are clarified.

The transfer function's *power series representation* exactly tells about the type and strength of the included non-linearities. The n-th power addend in the power series of $f(x)$ leads to a $\sin^n(y)$ term in the response, introducing – as shown above – harmonical contributions with

frequencies up to $n\omega_0$. But, if the power series contains all addends with powers between $n = 1$ and $n = N$, this does not necessarily mean that the response contains *all* higher harmonics up to $N\omega_0$: $\sin^n(\omega_0 t)$ brings along harmonical oscillations with the frequencies $(n - 2k)\omega_0$ (for $k = 0 \ldots n$) and *different amplitudes and phases*. Hence, considering more than one power series addend, very special transfer functions resulting in cancellation of one or more harmonic terms are imaginable.

A much more definite conclusion of the discussion above is that if *all odd* or *all even* power series addends are *missing*, there will be *no* $m\omega_0$ contribution to the system's response with m odd or even, correspondingly. This fact is important to consider for *odd* transfer functions (symmetric with respect to the origin; $f(x) = -f(-x)$) and *even* transfer functions (symmetric with respect to the $x = 0$ axis; $f(x) = f(-x)$): an even function's power series only contains even power terms and an odd function is constituted of only odd power terms.

A harmonic excitation as considered here ($A_0 = 0$) keeps the transfer function's symmetry with respect to an axis or the origin (the excitation takes place symmetrically around the point of symmetry), leading to a response $f(x(t))$ with the same symmetry. As argued, **this results in *only odd* or *only even* higher harmonics in the response.**

2.5.2 Ferrofluid magnetization response

The physical basis of MPI is the magnetization response $M(H(t))$ of magnetic nanoparticles constituting a ferrofluid. In the picture of non-linear response theory, the input is the magnetic field H (at the ferrofluid's place), changing over the time t. The ferrofluid's magnetization curve $M(H)$ is the transfer function. While input and output are known, **in MPS, the sample's magnetization curve is the unknown quantity.** FOURIER analysis of a sample's magnetization response to a harmonical excitation gives information about the transfer function's (i.e. $M(H)$'s) shape (power series representation), as explained in 2.5.1. **This information answers or at least helps to answer questions about the *existence* and *type* of magnetic particles in the in-**

vestigated sample.[1]

Transfer function: symmetry, non-linearity and Taylor series

For a classical magnetic system like a ferrofluid, it is reasonable that $M(H) = -M(-H)$ must always be true, because this is the one-dimensional representation of a magnetization following the magnetic field direction. Thus, $M(H)$ is always symmetric with respect to the origin. As explained in part 2.4.3, the magnetization curve of a ferrofluid constituted of noninteracting particles basically follows the LANGEVIN function. A $\coth(\alpha) - 1/\alpha$ shape of course features this origin symmetry, because both addends do. As a consequence, the power series expansion consists of only odd-order addends:

$$\begin{aligned}\mathcal{L}(\alpha) &= \coth(\alpha) - \frac{1}{\alpha} \\ &\approx \frac{1}{3}\alpha - \frac{1}{45}\alpha^3 + \frac{2}{945}\alpha^5 - \frac{1}{4725}\alpha^7 + \mathcal{O}(\alpha^9)\end{aligned} \tag{2.33}$$

Equation 2.33 is the TAYLOR expansion around $\alpha = 0$. At this point, the first-order contribution and the first non-linear term are in a ratio of 15. An expansion around $\alpha_{max} = \pm 1.37225$ results in a ratio of 4.5, i.e. here the non-linearity carries more than three times more weight. α_{max} is the numerical solution of

$$\frac{d^3}{d\alpha^3}\mathcal{L}(\alpha) = 0, \tag{2.34}$$

solving the problem

$$\alpha_{max} = \max\left(\left|\frac{d^2}{d\alpha^2}\mathcal{L}(\alpha)\right|\right). \tag{2.35}$$

Around α_{max}, the LANGEVIN function has the highest curvature and, hence, exhibits the most non-linearity. This can be exploited by an excitation of the system around α_{max}, leading to strong higher harmonic generation. Incidentally, it should be remarked here, that a power series

[1] In MPI, this is valid, too, but there it is the goal to obtain the information *locally* and the *local* magnetization curve is the big unknown, as will be described later.

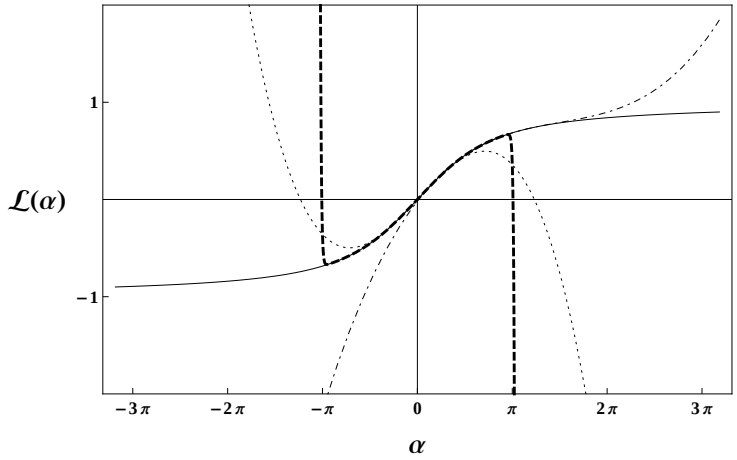

Figure 2.4: Solid line: Langevin function $\mathcal{L}(\alpha)$. Thick dashed line: TAYLOR series expansion of 99th order around $\alpha_0 = 0$: perfect convergence on the interval $]-\pi, \pi[$, strong divergence beyond. Dashed line: 3rd-order series around $\alpha_0 = 0$. Dotdashed line: 3rd-order series around $\alpha_0 = \pi$.

expansion around $\alpha \neq 0$ introduces even-order terms, due to lost symmetry.

Now, the reader may think that a simple calculation with the nth-order TAYLOR series of the magnetization curve enables to predict the higher harmonic contributions up to $n\omega_0$ in a ferrofluid's magnetization response for harmonical input. This is only true for distinct field strength intervals, because $\mathcal{L}(\alpha)$ is *not* an *entire* function: the TAYLOR series of $\mathcal{L}(\alpha)$ is *not* converging globally due to singularities in the complex plane at $m\pi\mathrm{i}$ with $m = -\infty, \ldots, -2, -1, 1, 2, \ldots, \infty$.

The TAYLOR series expansion around α_0 converges to $\mathcal{L}(\alpha)$ only for

$$|\alpha - \alpha_0| < r, \tag{2.36}$$

with r being the radius of convergence. r is given by the distance between α_0 and the *nearest* singularity to α_0 in the complex plane. For $\alpha_0 = 0$, the first equally near singularities are at $\pm\mathrm{i}\pi$. In this case the radius of convergence r is π. For $\alpha \in \mathbb{R}$ and $\alpha \notin]-\pi, \pi[$, the series *strongly* diverges from $\mathcal{L}(\alpha)$, no matter how many addends are considered. $\mathcal{L}(\alpha)$ and its TAYLOR series expansion around $\alpha_0 = 0$

for $n = 3$ and $n = 99$ are visualized in Figure 2.4. Additionally, a third-order expansion around $\alpha_0 = \pi$ is shown.

In MPS, it is possible to keep the magnetic field strength in a distinct interval so that α stays within an interval of convergence. Then, with the nth-order approximation (series) of the correct magnetization theory, it is possible to calculate the higher harmonic amplitudes up to the frequency limit $n\omega_0$. In MPI, as will be explained soon, quite big field strengths are used to reach the saturation state; in both directions of the magnetization curve. Then, no mutual interval of convergence can be found and a calculation with the power series expansion of the magnetization curve is senseless, because it does not represent physics anymore. Unfortunately, **this circumstance extremely complicates and obstructs an analytical discussion of image reconstruction schemes in MPI.**

Excitation: magnetic field irradiation

In MPS, a whole sample is excited *harmonically* and *homogeneously* by an oscillating magnetic field. Since the magnetic field has a direction, the most general approach is vector-based. $\vec{H}(t)$ is location-independent in the sample's volume and generally given by

$$\vec{H}(t) = \vec{H}_{off} + \vec{H}_{exc}\sin(\omega_0 t). \tag{2.37}$$

$\vec{H}_{off}$, the *static offset field* is of crucial relevance. First of all, an excitation with $|\vec{H}_{off}| \neq 0$ is breaking the symmetry of the response with respect to the origin, resulting in the occurrence of even higher harmonics, besides the odd ones. Furthermore, it can be used to maximize the generation of higher harmonics, as explained in the part before. As will be explained in part 2.6, neat spatial variation of the offset field is used to spatially resolve the magnetization response, leading to the *imaging capability* in MPI. All this is easy to understand for $\vec{H}_{off} \parallel \vec{H}_{exc}$. Then, only $|\vec{H}_{off}|$ and $|\vec{H}_{exc}|$ have to be considered, allowing a one-dimensional discussion. In all other cases $\sphericalangle(\vec{H}_{off}, \vec{H}_{exc}) \neq z\pi$ (with $z \in \mathbb{Z}$), the situation gets more complex and may exhibit exploitable advantages, as will be discussed shortly in part 4.3.1, considering $\vec{H}_{off} \perp \vec{H}_{exc}$. This topic is also treated in [18].

Response: inductive detection of the MPS signal

After thinking about a vector-based excitation model, a vector-based discussion of the magnetization response is required for integrity. This is conditioned by three decisive points/assumptions:

- The magnetization $\vec{M}(t)$ at the time t is always aligned with the irradiated magnetic field's direction $\vec{H}(t)$. This is true, as long as the excitation period $1/\omega_0$ is much bigger than the superparamagnetic relaxation time (see part 2.3.2).
- The absolute value of the magnetization $|\vec{M}(t)| \equiv M$ depends on the absolute magnetic field strength $|\vec{H}(t)| \equiv H$ as given by the magnetization curve $M(H)$.
- Inductive measurement by a coil only detects one magnetization dimension: the projection along the coil's axis.

This is leading to the general relation

$$\vec{M}(t) = M(|\vec{H}(t)|) \cdot \frac{\vec{H}(t)}{|\vec{H}(t)|}, \tag{2.38}$$

with the sample's magnetization curve $M(H)$. The measurable signal, an induced voltage $U(t)$, is governed by

$$U(t) \propto \frac{d}{dt} M_{coil}(t), \tag{2.39}$$

where M_{coil} is the magnetization component aligned with the coil. In the following discussion, $M_{coil}(t) = M(t)$ is assumed. $U(t)$ is from now on called the MPS/MPI signal.

The one-dimensional chain of excitation, transfer function, magnetization response and its time derivative is visualized in Figure 2.5 for $|\vec{H}_{off}| = 0$. The response's degree of distortion can be estimated best by means of the time derivative, which is clearly not harmonic anymore (the derivative of a harmonic signal would be harmonic, again). Everything in the figure was obtained analytically:

$$\begin{aligned} U(t) \propto \frac{d}{dt} M(t) &\propto \frac{d}{dt} \mathcal{L}(A \sin(\omega_0 t)) \\ &= \frac{\omega_0 \cot(\omega_0 t)}{A \sin(\omega_0 t)} - \frac{A\omega_0 \cos(\omega_0 t)}{\sinh^2(A \sin(\omega_0 t))}, \end{aligned} \tag{2.40}$$

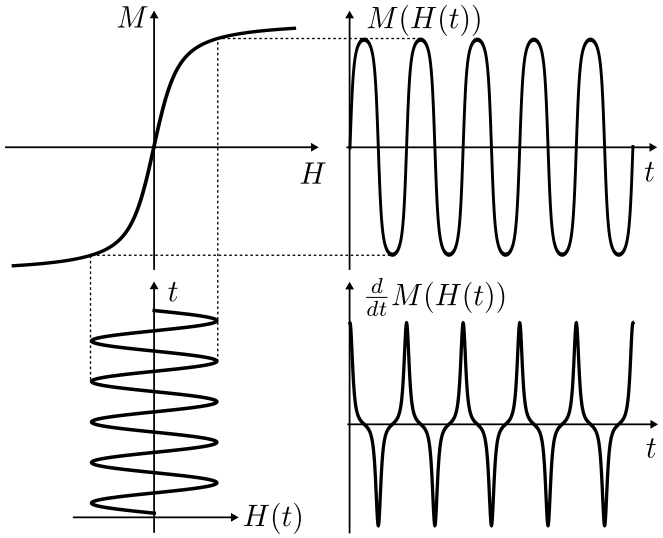

Figure 2.5: Magnetic excitation with $H_{off} = 0$ (bottom left). Transfer function $M(H)$ (top left). Magnetization response $M(H(t))$ (top right). Response's time derivative, which is proportional to measurable voltage $U(t)$, which is the MPS signal (bottom right).

with $A = 6$ and $\omega_0 = 1$.

Fourier analysis of the MPS signal

The next step is to obtain the detected signal's frequency spectrum, i.e. resolving the harmonic contributions and their amplitudes. Therefore, the time signal has to be transformed into the frequency domain by a FOURIER transformation $\mathcal{F}$.

With the analytically gained MPS signal available (Equation 2.40), it seems natural to go on analytically to find the exact FOURIER series coefficients a_n and b_n (Equation 2.27) for the first few n. But the FOURIER series coefficients' calculation of Equation 2.40 can be considered as too difficult or even impossible[1], so the analytical discussion stops now.

Instead, $U(t)$ – no matter if it was gained synthetically (analytically/numerically) or in an experiment – is analyzed *numerically* using

[1] Solving the occurring integrals seemed too hard. This was not discussed further.

a *discrete* FOURIER transformation (DFT). Therefore, $U(t)$ has to be sampled with a specific rate f_{sample}, yielding a set of data points $U_i(t_i)$. Put simply, the DFT transforms $U_i(t_i)$ into $A_i(\omega_i)$, i.e. it resolves the complex amplitude A_i for a specific frequency ω_i. Details about parameter selection (which has to be done very carefully), frequency resolution, detection limits and general characteristics of a DFT will be found in the simulation part 4.1.1.

Before the DFT result of the synthetically generated MPS signal from Figure 2.5 is presented, this point is a good opportunity to answer an obvious question:

> "*We are interested in the frequency spectrum of* $M(t)$ *to get information about the magnetic properties of the investigated sample. How does the spectrum of* $M(t)$ *translate into the spectrum of* $\frac{d}{dt}M(t)$*?*"

To answer this question, the time derivative of the complex FOURIER series representation of a periodic function $A(t)$ with periodicity $T = 2\pi/\omega_0$ is analyzed via Equation 2.28:

$$\begin{aligned}\frac{d}{dt}A(t) &= \frac{d}{dt}\sum_{n=-\infty}^{\infty} c_n \mathrm{e}^{\mathrm{i}n\omega_0 t} = \sum_{n=-\infty}^{\infty} c_n \frac{d}{dt}\mathrm{e}^{\mathrm{i}n\omega_0 t} \\ &= \mathrm{i}\omega_0 \sum_{n=-\infty}^{\infty} n \cdot c_n \mathrm{e}^{\mathrm{i}n\omega_0 t} \end{aligned} \tag{2.41}$$

Of course, inductive detection does *not* change the signal's fundamental frequency (and, thus, does not produce other frequency contributions). But, the time derivative introduces a factor of $\mathrm{i}\omega_0 n = \mathrm{i}\omega$ to each FOURIER component. It so to say *amplifies* the higher harmonic contributions linearly with ω. This has an important consequence for *numerical* simulations of the MPS/MPI signal: the frequency spectrum of $\frac{d}{dt}M(t) \propto U(t)$ can be obtained by simply multiplying the frequency spectrum of $M(t)$ with $\mathrm{i}\omega$. Advantage: time-consuming numerical building of the time derivative is not necessary anymore. Additionally, the "$\mathrm{i}\omega$-method" turns out to be more accurate than the simplest numerical algorithms to build the derivative of a discrete data set.

Figure 2.6 shows the frequency spectrum of the MPS signal corresponding to the signal chain in Figure 2.5. Both presented methods to gain this spectrum were used:

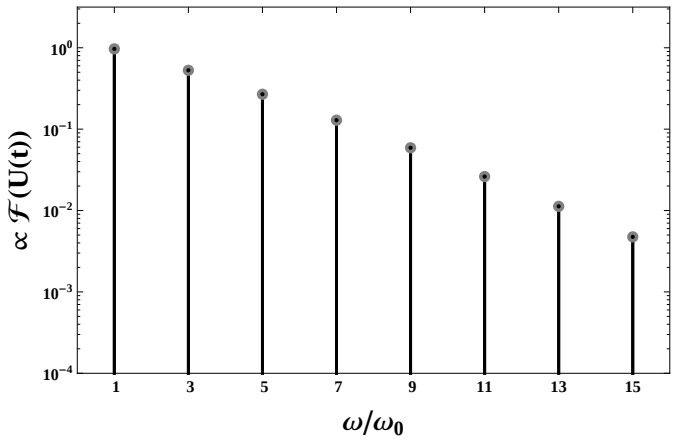

Figure 2.6: Semilogarithmic diagram of the MPS signal's FOURIER spectrum $\mathcal{F}(U(t))$; gained by DFT (absolute values shown). The black bars and dots are the result of $\mathrm{DFT}(\frac{d}{dt}M(t))$; the gray dots are the result of $\mathrm{i}\omega \cdot \mathrm{DFT}(M(t))$.

- sampling and DFT of the analytically gained $\frac{d}{dt}M(t)$
- sampling and DFT of $M(t)$; multiplication with $\mathrm{i}\omega$ afterward.

As expected, both results equal each other. Furthermore, Figure 2.6 is a visual proof, attesting the non-linear response theory considerations made above. It shows a *discrete* spectrum with *only odd* harmonics. The highest amplitude can be found in the fundamental contribution $\omega/\omega_0 = 1$; for higher n the amplitudes seem to decay almost exponentially (almost linearly in the semilogarithmic scale).

The MATHEMATICA source code calculating the data shown in Figure 2.6 can be found in Appendix A.1 (page 98).

Evaluation of the MPS signal's frequency spectrum

The single magnetic moments of a biological system (formed of water, cells and their constituents, big and small proteins, etc.) are *several orders of magnitude lower* than the giant magnetic moments of single-domain particles. As explained in part 2.3.4 ("para- vs. superparamagnetism"), such a system's magnetization behavior can be considered as

linear. This assumption is valid[1], especially for the low MPI/MPS excitation field amplitudes H_{exc}, which typically are on the order of $10\,\mathrm{mT}$. Therefore, MPI is often called *"background-free"*: *everything* else than giant magnetic moments, i.e. magnetic single-domain particles in their function as contrast agent *only* contributes to the fundamental harmonic with $\omega/\omega_0 = 1$. In other words, higher harmonics in the MPS signal's frequency spectrum *prove the existence* of contrast agent within the volume of interest. **So the prime information extractable from the MPS signal is whether there is contrast agent in the investigated volume or not.**

By performing a detailed analysis of the higher harmonic amplitudes, it is possible to make much more quantitative and definite statements. Consider a ferrofluid magnetization theory that *correctly* incorporates the effect of a whole set of variables like particle concentration, magnetic core diameter (distribution), core material, excitation frequency and amplitude (and maybe others) on the transfer function $M(H)$. Then – if all other quantities are known – it is possible to specify the value of an unknown variable from the higher harmonic amplitudes. In a way, MPS is an efficient way to sample the shape of the volume of interest's magnetization curve with high precision. On the other hand, this means that **MPS in combination with simulations is a promising tool to test a magnetization theory for validity if the whole set of variables is known!**

[1] The reader may have doubts and think of e.g. *hemoglobin* (the iron-containing oxygen-transport protein in the red blood cells) and *ferritin* (a protein storing and releasing iron in a controlled fashion). Hemoglobin indeed behaves para- or even diamagnetic [19], because it is exhibiting many *spatially separated* iron atoms, forming single atomic magnetic moments. Ferritin cores, which can accommodate up to 4500 Fe(III) atoms, have an average magnetic moment of ca. $100\,\mu_\mathrm{B} \approx \mathcal{O}(10^{-22})\,\mathrm{Am}^2$ [20], which still is several orders of magnitude lower than the magnetic moment of applied single-domain particles (e.g. $10^{-18}\,\mathrm{Am}^2$ for single-domain magnetite cores with 16 nm diameter). If both are in the investigated volume at the same time, the latter ones simply outstrip the higher harmonic contributions of ferritin by orders of magnitude. Nevertheless, it at least theoretically seems to be possible to use ferritin as contrast agent itself, by exploiting its *extremely low* non-linear magnetization behavior.

2.6 Magnetic Particle Imaging

In MPI, it is the goal to measure the spatial distribution of contrast agent in a sample's volume (volume of interest, **VOI**), i.e. the contrast agent's particle density ρ at location $\vec{x}$.

For the step from MPS to MPI, the MPS signal has to be spatially encoded, i.e. it has to be detected and evaluated for a small sub-volume of the VOI. For realizing this, the basic idea is to apply a spatially dependent offset field $H_{off}(\vec{x})$ to the sample: $|H_{off}|$ is zero in a so-called *field-free point* (**FFP**), but raises extremely fast with increasing distance from the FFP, resulting in **a strong offset field everywhere, except in the FFP and its near vicinity.** By doing this, the contrast agent in the major part of the sample's volume is magnetically *saturated*, which is "switching off" higher harmonics from this VOI's part, as will be shown in part 2.6.1. If the whole VOI gets excited in this configuration, the emitted signal tells about contrast agent only in the FFP and its near vicinity; the rest of the sample is *masked out*.

By moving the FFP – using a temporally dependent offset field $H_{off}(\vec{x}, t)$ – it is possible to scan the whole VOI [1]. $\rho(\vec{x})$, the "image", can then be obtained by acquiring the emitted signal over the time, followed by an image reconstruction scheme. The specific reconstruction algorithm depends on the actual signal acquisition method. Two of these methods and their corresponding reconstruction schemes will be introduced in parts 2.6.2 and 2.6.3.

A conceivable extension of the FFP principle is to realize spatial encoding using a *field free line* (**FFL**). This implicates averaging and results in a higher signal to noise ratio per overall acquisition time, as pointed out in [21]. The FFL approach will not be discussed further in this thesis.

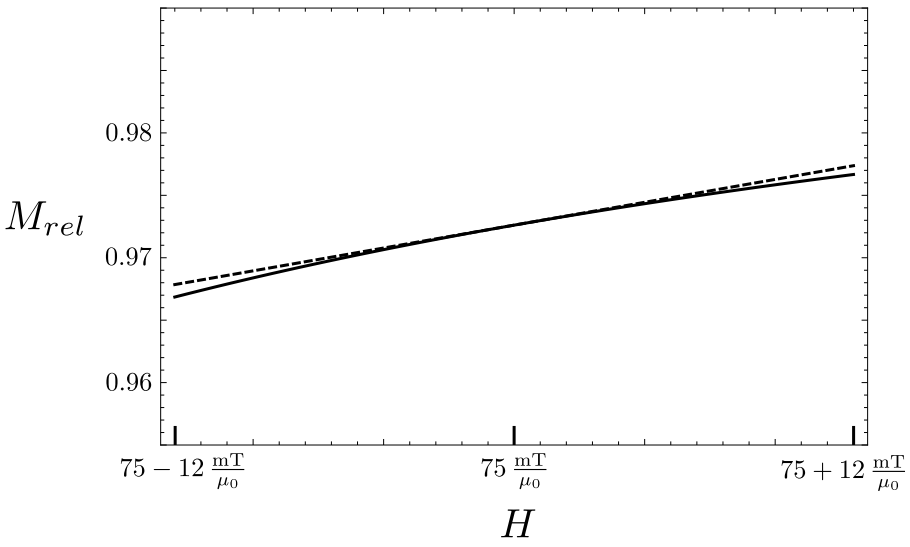

Figure 2.7: Solid line: a ferrofluid's relative magnetization curve $M_{rel}(H)$, described by $\mathcal{L}(35 + 6\sin(t))$, which actually represents magnetite particles with $d = 20\,\mathrm{nm}$, excited by $H(t) = 75\,\mathrm{mT}/\mu_0 + 12\,\mathrm{mT}/\mu_0 \cdot \sin(t)$. Dashed line: linear approximation of the curve for $H = 75\,\mathrm{mT}/\mu_0$.

2.6.1 Offset field for spatial encoding: "switching off" higher harmonics

In Figure 2.6, the spectrum of the MPS signal $U(t)$ was shown. There, $U(t)$ is proportional to $\frac{d}{dt}\mathcal{L}(6\sin(t))$ (compare to Equation 2.40). To give the reader a feeling for actual physical quantities behind this simple mathematical representation, this corresponds to a ferrofluid sample made of magnetite cores ($M_s = 4.8 \cdot 10^5\,\mathrm{A/m}$ [22]) with a diameter $d = 20\,\mathrm{nm}$, excited harmonically by a magnetic field $H(t) = 12\,\mathrm{mT}/\mu_0 \cdot \sin(t)$ at temperature $T = 300\,\mathrm{K}$.

Consider this setup with an additionally applied offset field $H_{off} = 75\,\mathrm{mT}/\mu_0$. Before showing the spectrum of the signal $U(t)$ – now simply represented by $\frac{d}{dt}\mathcal{L}(35 + 6\sin(t))$[1] – a closer look to the relevant "cut-out" of the system's relative magnetization curve $M_{rel}(H)$ is useful. It is shown in Figure 2.7: the shape is almost **linear**, because H is in the sample's regime of magnetic saturation, where M_{rel} is almost constant.

[1] LANGEVIN parameter $\alpha = \mu_0 H m(d)/kT$ is ∼35 for the H_{off}, d, M_s, T given.

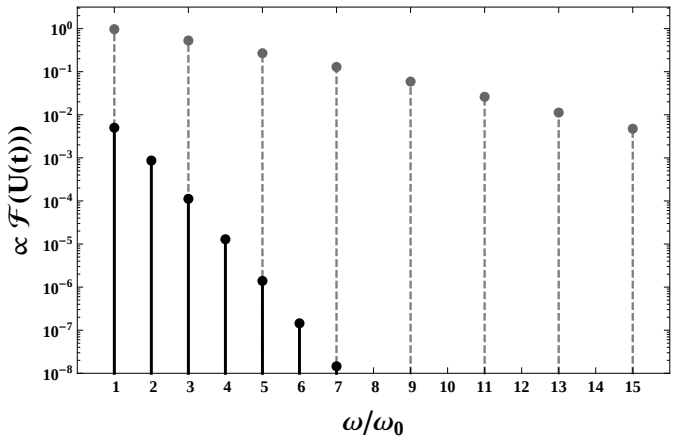

Figure 2.8: Semilogarithmic diagram of the MPS signal's FOURIER spectrum $\mathcal{F}(U(t))$; gained by DFT (absolute values shown). The black bars and dots are the result of $\mathrm{DFT}(\frac{d}{dt}\mathcal{L}(35 + 6\sin(t)))$ (corresponding to a sample within an offset field); the gray bars and dots are the result of $\mathrm{DFT}(\frac{d}{dt}\mathcal{L}(6\sin(t)))$ (without offset field).

Figure 2.8 shows the strong impact of the considered offset field on the amplitudes of the single harmonics:

- The fundamental harmonic drops by more than two orders of magnitude: the relevant magnetization curve cut-out is almost constant, so $\frac{d}{dt}M(t)$ drops significantly.
- Due to lost symmetry with respect to the origin of the magnetization curve, *even* harmonics appear.
- The third higher harmonic decreases by almost four orders of magnitude. The seventh is reduced by even more than seven orders; the reduction raises extremely fast with increasing frequency.

"Switching off higher harmonics" is only a descriptive term, meaning the exceedance of an offset field strength *threshold*, above which the higher harmonic contributions are so low that they vanish within the noise of a real experimental setup. In other words, for spatial encoding in MPI, it is sufficient to suppress the higher harmonic amplitudes from

the sample volume's major part to a certain degree, so that the signal from the FFP and its vicinity is much higher. Therefore, $H_{off}(\vec{x}, t)$ is also called *selection field*.

For *ideal* spatial encoding, the offset field's spatial shape would exhibit steps, suppressing higher harmonics from everywhere else than the FFP. Since infinite magnetic field gradients do not exist, the threshold described above is reached only in some distance from the FFP. This is why *always* contrast agent in the FFP *and its vicinity* are responsible for the signal. The size of this vicinity depends on the offset field's slope in all different directions off space. The dependence of a specific higher harmonic's amplitude on the spatially changing offset field strength is leading to a *point spread function* (**PSF**) of certain shape and width for this specific harmonic.

2.6.2 Frequency Mixing Method

The most intuitive implementation of the scanning concept described above is to *slowly* steer the FFP through the VOI, while permanently exciting the whole volume by irradiating a *rapidly* oscillating magnetic field, as proposed in the initial MPI publication [1]. FFP steering is either done mechanically by moving the sample within a static selection field or by varying the magnetic field configuration over the time. The FFP movement's periodical repetition then defines a frequency which is small in contrast to the excitation frequency. Due to the two different occurring frequencies, *we* use the name *frequency mixing method* (**FMM**).

Consider a one-dimensional sample, with contrast agent density distribution $\rho(x)$. The simplest imaginable selection field is a spatially linear changing magnetic field (a magnetic field gradient, as produced by a MAXWELL coil pair). Relative movement of the selection field to the sample defines the FFP trajectory $x_{FFP}(t)$, as sketched in Figure 2.9. The actual trajectory – which might e.g. exhibit a constant or harmonic velocity $\frac{d}{dt}x_{FFP}(t)$ – is not of importance for now.

While moving the selection field, the whole sample is excited homogeneously and the emitted signal gets detected, yielding the time-dependent amplitude of the n-th harmonic, $A_n(t)$. Knowledge about the FFP's trajectory yields $A_n(x_{FFP})$. While this relation already allows

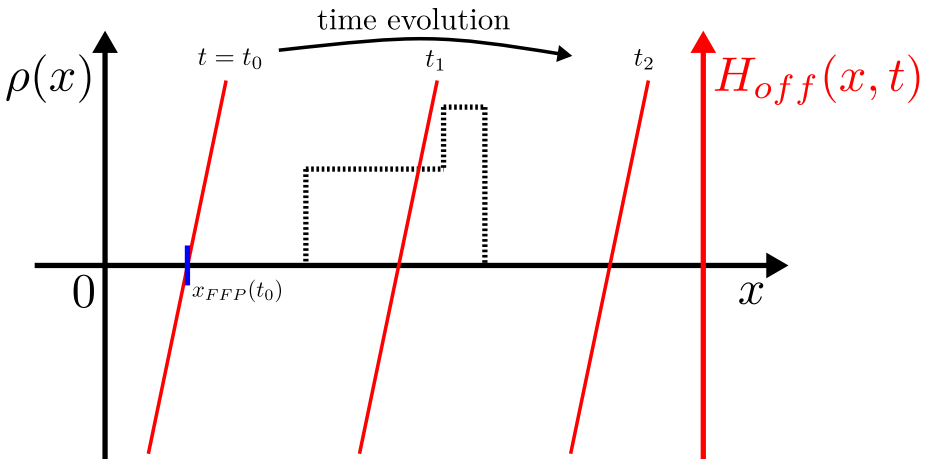

Figure 2.9: Black dashed line: 1D MPI sample/phantom (contrast agent density distribution $\rho(x)$). Red lines: Selection field (linearly increasing around FFP) for different points in time.

for qualitative statements about the contrast agent's spatial distribution, a more exact and quantitative *reconstruction* of $\rho(x)$ requires

- **deconvolution** of $A_n(x_{FFP})$ and the n-th harmonic point spread function $A_n(H_{off}(x))$ and
- a **calibration** of the system using a sample with known contrast agent density, yielding $A_n(\rho)$ which can be used to determine $\rho(A_n(x_{FFP}))$.

2.6.3 Drive Field Method

This method makes use of *extremely fast* FFP movement, i.e. movement of the "frequency mixing method's selection field" $H_{off}(\vec{x},t)$. Then, the magnetic field at a fixed point in space changes so quickly, that voltage induction by the emitted magnetization response is as strong as due to the excitation field's oscillation in the frequency mixing method's framework. Hence, the additional excitation field is obsolete. Instead, a *static* selection field (exhibiting an FFP) is considered, *driven* (moved) through the VOI by a superimposed rapidly oscillating **drive field**, specifying the FFP's trajectory $\vec{x}_{FFP}(t)$. Hence, Figure 2.9 is suitable for this method's illustration, too.

Using this method, which was also introduced in [1], a scan of the whole VOI takes a lot less time than using the frequency mixing method. With respect to a well-established terminology (that the selection field/FFP is "driven" by a "drive field"), *we* call this method *drive field method* (**DFM**).

While the FMM is easier to realize in an experiment, the DFM is the method that allows for MPI real-time applications. Therefore, at the moment, it is the method of choice when constructing an MPI scanner, which should be able to compete with other imaging techniques like MRI. Actually, PHILIPS is currently building up a 3D MPI scanner for mice, implementing the DFM [2]. On that account, *our* DFM reconstruction scheme – as it is used in a simulation presented in part 4.3.2 – is discussed in some detail now.

DFM reconstruction scheme

To be able to calculate an image from a time signal obtained by the DFM, the MPI system's transformation behavior – also called **system function** – has to be known. The corresponding *inverse* transformation applied to a measured signal then accomplishes image reconstruction. This abstract description becomes much more comprehensible by considering an actual mathematical formalism, which is the intention of the next paragraphs.

The mathematical formalism introduced here is based on *linear algebra*: signal/time and density/space information gets discretized and finds its representation in *vectors*, while the system function is formed by a *matrix* operator $\mathbf{S}$. The operator $\mathbf{S}$, applied to a *contrast agent density distribution vector*, results in an *MPI time signal vector*. Consequently, the inverse operator $\mathbf{S^{-1}}$ can be used to transform a measured time signal vector into a contrast agent density distribution vector. The basic principle to determine $\mathbf{S}$ is the following:

1) Discretize the VOI in N small sub-volumes (smaller than the desired image resolution), numbered by $i = 1, 2, \ldots, N$.

2) Form a "delta sample": fill sub-volume i with contrast agent of *known* density ρ_0.

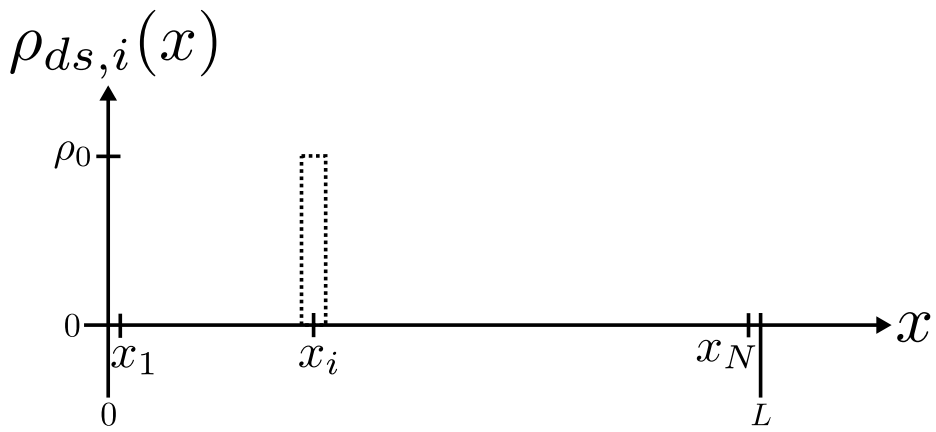

Figure 2.10: "1D VOI" of length L, discretized to N sub-volumes with the centers $x_{1...N}$. Dashed line: a *delta sample's* contrast agent density distribution $\rho_{ds,i}(x)$: density ρ_0 in the i-th sub-volume and zero everywhere else.

3) Run the full FFP trajectory and sample the emitted signal. The vector of sampled values defines column i of $\mathbf{S}$.

4) Repeat steps 2 and 3 for all i to obtain entire $\mathbf{S}$.

These steps are explained now, using detailed mathematical notation.

A "delta sample" with known contrast agent density ρ_0 in sub-volume i is continuously described by $\rho_{ds,i}(\vec{x})$, which is visualized for a "1D VOI" of length L in Figure 2.10. Due to the VOI's discretization, a delta sample's density distribution can just as well be given by the *vector* $\vec{\rho}_{ds,i}$: each of the N components corresponds to the contrast agent's density in *one* sub-volume (ρ_0 within the i-th sub-volume and zero everywhere else):

$$\vec{\rho}_{ds,i} = \begin{pmatrix} 0 \\ 0 \\ \vdots \\ \rho_0 \\ \vdots \\ 0 \end{pmatrix} \quad \text{with component numbers} \quad \begin{matrix} 1 \\ 2 \\ \vdots \\ i \\ \vdots \\ N \end{matrix} \tag{2.42}$$

Of course, this description is not limited to one dimension: all sub-volumes of a 3D VOI can be numbered consecutively, in the order given by the FFP trajectory $\vec{x}_{FFP}(t)$.

The continuous system's non-linear[1] signal part $A_{ds,i}(t)$ – produced by the corresponding delta sample $\rho_{ds,i}(\vec{x})$ – is acquired while driving the FFP along $\vec{x}_{FFP}(t)$. Discrete signal sampling yields M time signal data points, constituting the vector

$$\vec{A}_{ds,i} = \begin{pmatrix} A_{ds,i,1} \\ A_{ds,i,2} \\ \vdots \\ A_{ds,i,M} \end{pmatrix}. \tag{2.43}$$

This signal vector can be of arbitrary length M: the whole FFP trajectory must be driven at least once, but there is no upper limit.

The signal $\vec{A}_{ds,i}$ defines the i-th column of the $M \times N$ matrix $\mathbf{S}$ (all other columns are "disabled" by the zeros in $\vec{\rho}_{ds,i}$):

$$\begin{array}{ccccc} \vec{A}_{ds,i} & = & \mathbf{S} & \cdot & \vec{\rho}_{ds,i} \end{array}$$

$$\begin{pmatrix} A_{ds,i,1} \\ A_{ds,i,2} \\ A_{ds,i,3} \\ A_{ds,i,4} \\ A_{ds,i,5} \\ \vdots \\ A_{ds,i,M} \end{pmatrix} = \frac{1}{\rho_0} \cdot \begin{pmatrix} \cdots & \cdots & A_{ds,i,1} & \cdots & \cdots \\ \cdots & \cdots & A_{ds,i,2} & \cdots & \cdots \\ \cdots & \cdots & A_{ds,i,3} & \cdots & \cdots \\ \cdots & \cdots & A_{ds,i,4} & \cdots & \cdots \\ \cdots & \cdots & A_{ds,i,5} & \cdots & \cdots \\ \cdots & \cdots & \vdots & \cdots & \cdots \\ \cdots & \cdots & A_{ds,i,M} & \cdots & \cdots \\ 1 & \cdots & i & \cdots & N \end{pmatrix} \cdot \begin{pmatrix} 0 & 1 \\ \vdots & \vdots \\ \rho_0 & i \\ \vdots & \vdots \\ 0 & N \end{pmatrix} \tag{2.44}$$

Hence, after completing step four from the list above, the system function $\mathbf{S}$ can be assembled by putting together the N column vectors

[1] I.e. $A_{ds,i}(t)$ must not contain the linear response, which can be accomplished by e.g. analog filtering of the fundamental harmonic.

$\vec{A}_{ds,1\ldots N}$:

$$\mathbf{S} = \frac{1}{\rho_0} \begin{pmatrix} \vec{A}_{ds,1} & \vec{A}_{ds,2} & \cdots & \vec{A}_{ds,N} \end{pmatrix} \tag{2.45}$$

The entire operator $\mathbf{S}$ predicts the signal vector $\vec{A}$ for an arbitrary sample $\vec{\rho}$ and, thus, $\mathbf{S^{-1}}$ can be used to calculate the contrast agent density distribution of an unknown sample from the measured time signal:

$$\begin{aligned} \vec{A} &= \mathbf{S}\vec{\rho} \\ \vec{\rho} &= \mathbf{S^{-1}}\vec{A} \end{aligned} \tag{2.46}$$

Two important remarks have to be made about this method:

- This is a linear reconstruction method, presuming the MPI signal's amplitudes A being *linearly* related to the contrast agent's density ρ. If this assumption does not match physics, *quantitative* reconstruction of ρ values *fails* to a certain degree using this method[1].
- $\mathbf{S}$ commonly is a rectangular matrix, so numerical methods to build the *pseudoinverse* have to be applied. Numerical stability of this operation is not guaranteed, especially in case of strong noise. Furthermore, $\mathbf{S}$ can get very big, leading to high computing requirements. Consider a 3D VOI divided into $64 \times 64 \times 64$ subvolumes, yielding $N = 262,144$. E.g. $M = 4096$ time sampling points acquired during FFP movement then result in a matrix with 10^9 entries. Numerical inversion of such huge matrices requires a lot of random access memory. Fortunately, for a fixed MPI scanner's configuration, determination of $\mathbf{S}$ and calculation of $\mathbf{S^{-1}}$ have to be accomplished only once.

[1] MPI using the FMM is not better at this point: deconvolution methods are linear operators, too.

Chapter 3

Theory of particle interaction and polydispersity

As shown in the last chapter, for comprehension of the MPI signal's generation in a *non-ideal* world, it is required to have knowledge of the impact of two vitally important facts:

- Common ferrofluids consist of *polydisperse* particles, i.e. they exhibit a magnetic core diameter probability distribution function $p(d)$ as defined in 2.4.1.
- Dense ferrofluids feature particle densities exceeding the (extremely) small scope of validity of the SPM (see 2.4.3). In that case, magnetic interparticle coupling leads to deviations from the SPM.

In this chapter, part 3.1 describes the impact of different particle sizes and then introduces two possible parameterizations of $p(d)$. Part 3.2 discusses the dependency of the magnetization curve the on particle density ρ and introduces a promising magnetization theory, incorporating the effect of increasing ρ.

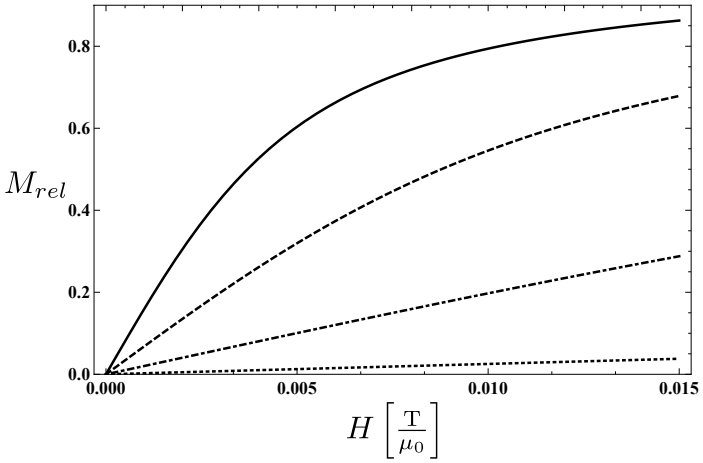

Figure 3.1: Relative magnetization of a monodisperse ferrofluid $M_{rel}(H)$ for different magnetic core diameters d (as given by $\mathcal{L}(m(d)\mu_0 H/kT)$ with $T = 300\,\mathrm{K}$ and $m(d)$ as Equation 2.14 with magnetite's M_s [22]). Dotted line: $d = 5\,\mathrm{nm}$, dotdashed line: $d = 10\,\mathrm{nm}$, dashed line: $d = 15\,\mathrm{nm}$, solid line: $d = 20\,\mathrm{nm}$.

3.1 Polydispersity of magnetic particles

3.1.1 Impact of different particle sizes

The initial slope of the relative magnetization of a monodisperse ferrofluid

$$\left.\frac{\partial M_{rel}}{\partial H}\right|_{H=0} = \frac{\chi_{init}}{M_\infty} \quad \text{with} \quad M = M_\infty M_{rel} \tag{3.1}$$

is directly proportional to the magnetic moment m of the particles the fluid is constituted of: due to Equation 2.33, $\mathcal{L}(\alpha)$ has an initial slope of $\alpha/3$. For constant magnetic field and temperature, α itself is directly proportional to m, as given by Equations 2.10 and 2.11. The magnetic moment of a particle is linearly related to its magnetized volume and with that proportional to d^3 (cf. Equation 2.14), yielding

$$\frac{\chi_{init}}{M_\infty} \propto d^3. \tag{3.2}$$

This relation is demonstrated in Figure 3.1. There, relative magnetization curves for $d = 5, 10, 15, 20\,\mathrm{nm}$ are shown. χ_{init}/M_∞ for

$d = 20\,\text{nm}$ is 64 times larger than χ_{init}/M_∞ for $d = 5\,\text{nm}$, illustrating the fact that the regime of saturation ($M_{rel} \to 1$) is reached for *much* lower field strengths with increasing d. This in turn results in a much more non-linear shape of the magnetization curve within the considered magnetic field range (cf. 3.1). As explained in section 2.5, this has **drastic impact on the generation of higher harmonics within the MPS/MPI signal.** A more quantitative investigation is accomplished via simulations in part 4.2.1.

In a polydisperse ferrofluid, the different magnetization curves superimpose to an effective one, with their weights corresponding to their relative fraction, as given by the magnetic core diameter probability distribution function $p(d)$.

3.1.2 Parameterization of magnetic core diameter distributions

For simulating the magnetization response of a polydisperse ferrofluid, it is necessary to parameterize the magnetic core diameter distribution mathematically. The most intuitive and convenient approach is to describe it by a function with only two parameters – *mean value* and *width* of the distribution.

But which two-parametrical function matches a *real* distribution best? Here, many authors refer to the *lognormal* distribution [23] (1975). The lognormal distribution is considered in current MPI literature as well [24, 25]. Another possible parameterization – which most often occurs in theoretical publications – is an *exponentially damped power function*, as used in [26]. Both functions and their properties will now be introduced, followed by a comparative discussion.

The lognormal distribution

The lognormal distribution $p_1(x)$ with the parameters S and μ is

$$p_1(x) = \frac{1}{\sqrt{2\pi}Sx}\,\mathrm{e}^{-\frac{(\ln x-\mu)^2}{2S^2}}. \tag{3.3}$$

The maximum is reached for

$$x_{max} = \mathrm{e}^{\mu-S^2}, \tag{3.4}$$

the n-th moment of the distribution is

$$\langle x^n \rangle = \mathrm{e}^{\frac{1}{2}n^2S^2+n\mu}. \tag{3.5}$$

The expected value E and variance V are

$$E = \langle x \rangle = \mathrm{e}^{\frac{1}{2}S^2+\mu} \tag{3.6}$$

$$V = \int_0^\infty (x - \langle x \rangle)^2 p_1(x) \mathrm{d}x = \mathrm{e}^{S^2+2\mu}(\mathrm{e}^{S^2} - 1). \tag{3.7}$$

Exponentially damped power function ("gamma distribution")

The exponentially damped power function distribution $p_2(x)$ with the parameters x_0 and α is

$$p_2(x) = \frac{x_0^{-\alpha-1}}{\Gamma(1+\alpha)}\, x^\alpha \mathrm{e}^{-\frac{x}{x_0}}. \tag{3.8}$$

Due to the Γ-function in the normalization term, this distribution is often called "gamma distribution". The maximum is at

$$x_{max} = x_0\alpha, \tag{3.9}$$

the n-th moment of the gamma distribution is

$$\langle x^n \rangle = \frac{\Gamma(1+n+\alpha)}{\Gamma(1+\alpha)} x_0^n. \tag{3.10}$$

Expected value and variance are

$$E = x_0(1+\alpha) \tag{3.11}$$

$$V = x_0^2(1+\alpha). \tag{3.12}$$

Properties and justification in comparison

While S, μ, α and x_0 do not have a special meaning, the relations noted above can be used to express $p_1(x)$ and $p_2(x)$ in dependence of E and V (using $S(E,V)$, $\mu(E,V)$, $\alpha(E,V)$ and $x_0(E,V)$). Both distributions are visualized for two specific sets of E and V in Figure 3.2. Qualitatively, both distributions look very similar.

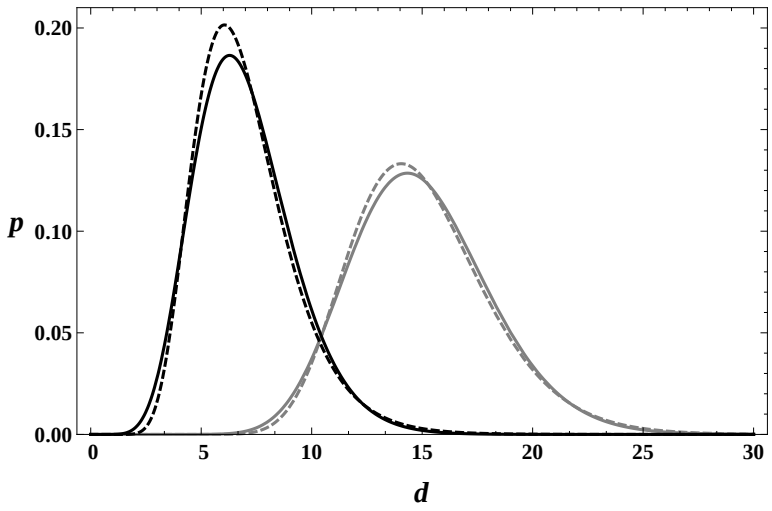

Figure 3.2: Gamma (solid) vs. lognormal (dashed) distribution for two parameter sets: $E = 7$, $V = 5$ (black) and $E = 15$, $V = 10$ (gray).

Modeling reality with distribution functions like the ones introduced above is based on quite bad arguments. There is no specific reason why ferrofluid particle size distributions should either follow this or that mathematical function. The actual choice of the function does not even depend on the method of producing the particles [27]. The only definite constraints are:

- $p(d)$ must converge to zero for $d \to 0$.
- The distribution must have *only one* maximum (the manufacturing process is assumed to work like that: the probability to create a particle of certain size drops with increasing difference to the predominantly produced particle size).
- The location of the maximum and the strength of the decay to its sides must be adjustable with two parameters.

All this is fulfilled for both the lognormal and gamma distribution.

To check if a mathematical distribution matches reality, comparison with experiments is required. Information about the *magnetic core* sizes can only be obtained by magnetization measurements, leading to

a vicious circle, as will be explained in the next part. The following methods help to measure *geometrical* particle sizes:

- Photon correlation spectroscopy (**PCS**, based on dynamic light scattering [28]) is capable of determining the *hydrodynamic diameter* distribution profile of particles in a suspension. Hence, this method measures the *entire* particle size (*including shell* in case of ferrofluids).
- In transmission electron microscopy (**TEM**), the bulk core material changes electron intensity, but TEM almost does not "see" common particle shells (e.g. dextran); i.e. TEM allows to extract information about geometrical *bulk core* sizes from obtained images.

The objective is to make a statement about the *magnetic core* size d, which is the bulk core *less* the thin demagnetized layer (cf. 2.4.1). Hence, PCS is completely inappropriate at this point[1]. TEM yields usable but *not perfect* information: bulk and magnetic core size distributions differ and the extraction of size information from TEM images is imprecise. However, TEM seems to be the most suitable independent method for gathering statistical data about a size distribution that matches $p(d)$ well.

In [27], the authors considered TEM data of several magnetite ferrofluid samples. For each sample's data, they extracted the first and second moment and used them to fit lognormal and gamma distributions, so that mean value and variance of both functions coincided with experimental data. Comparison of higher order moments of the two fitted distribution functions to corresponding moments of the TEM data revealed that the moments of higher order of the lognormal distribution strongly overshoot the real moments (e.g. by a factor 2-3 for the sixth moment), while the moments of the gamma distribution seem to match reality much better[2]. The difference between the higher order moments of both distribution functions is visualized in Figure 3.3.

[1] Often, the shell of a magnetic particle is much thicker than the magnetic core itself. Therefore and due to shell thickness variations, it is much too unreliable to correlate magnetic core diameter and hydrodynamic diameter.

[2] The exponential decay of the gamma distribution for big arguments is stronger than the one of the lognormal distribution.

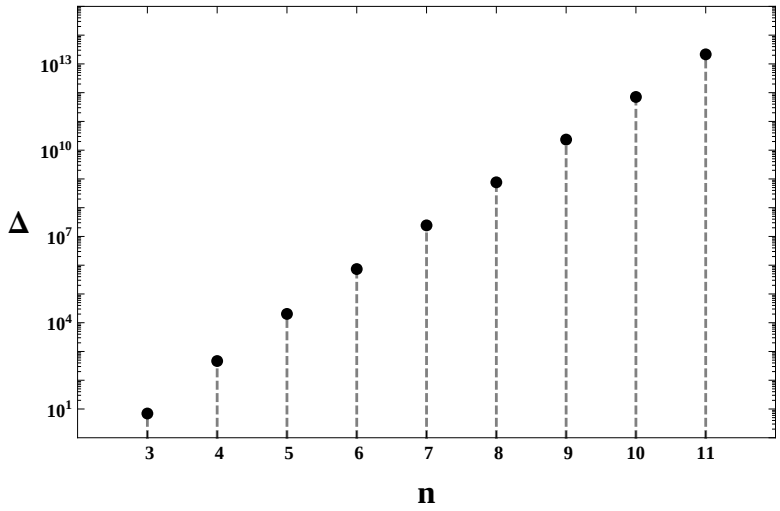

Figure 3.3: Difference Δ between n-th moment ($\langle x^n \rangle$) of lognormal distribution and the n-th moment of the gamma distribution for $E = 15$ and $V = 10$ (as shown in Figure 3.2).

Considering $\chi_{init} \propto M_\infty d^3$ (cf. Equation 3.2) and $M_\infty \propto m(d)$ leads to

$$\chi_{init} \propto d^6. \tag{3.13}$$

Thus, for predicting the magnetic properties of a ferrofluid, the accuracy of $p(d)$ in higher order moments is essential. Therefore, the gamma distribution is the preferable choice, which clearly should be adopted in the field of MPI, too.

3.2 Magnetic particle coupling in dense ferrofluids

3.2.1 Impact of interparticle coupling

As pointed out in 2.4.3, the single particle model is valid only for particle densities $\rho \to 0$. With increasing ρ, a single magnetic moment is affected more and more by surrounding magnetic moments via dipole-

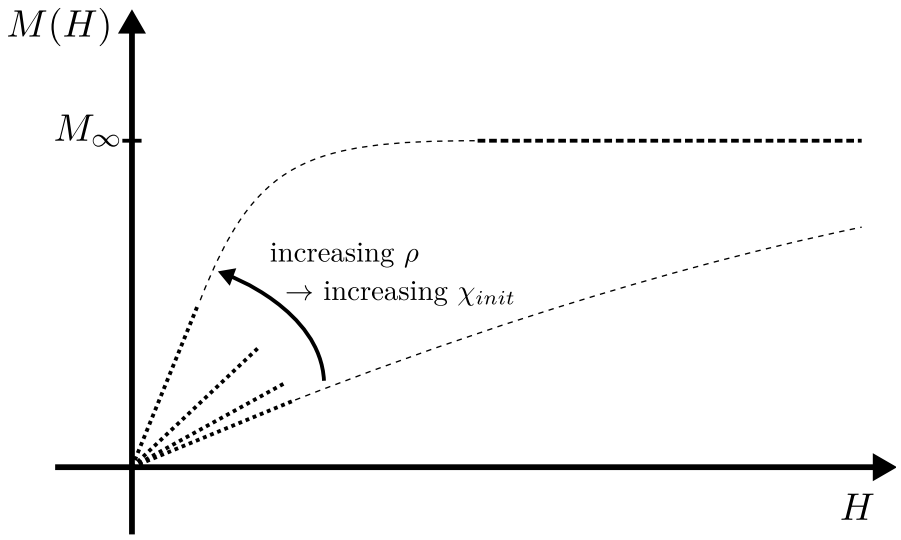

Figure 3.4: Visualization of the impact of increasing local particle density ρ on a ferrofluid's magnetization curve: the initial susceptibility χ_{init} increases with ρ, while the saturation magnetization M_∞ is *constant* (it only depends on the absolute amount of substance in the volume of interest, which is not changed by local ρ variations).

dipole interaction. The impact of this effect on the magnetization curve of a ferrofluid is assessable:

- The saturation magnetization M_∞ is reached when all magnetic moments are aligned with the external field. Hence, it is *not* affected by particle density variations. It only depends on the absolute amount of magnetic substance within the volume of interest.
- Single magnetic moments "seeing each other", support each other in the process of alignment. Thus, increasing ρ leads ti a steeper magnetization curve and saturation is reached for a weaker external magnetic field.
- The point above implies the magnetization curve $M(H, \rho)$ being *non-linear* dependent on ρ (in contrast to the SPM, cf. part 2.4.3). In particular, χ_{init} is increasing with ρ, which is verified experimentally in [29].

This coherence is visualized in Figure 3.4.

From the discussion above it is clear that the particle density ρ must have huge impact on the amplitudes of the higher harmonics within the MPI/MPS signal: increasing ρ leads to a larger curvature of $M(H)$ which means *stronger non-linearity* and – with that – **stronger generation of higher harmonics.** Furthermore, the effect of increasing particle concentration on the magnetization curve of a ferrofluid qualitatively is very **similar to the effect of increasing particle diameters**: both result in higher χ_{init} and – with that – stronger non-linearity and higher harmonic generation.

3.2.2 Magnetization theories for concentrated ferrofluids and magneto-granulometric analysis

Development of a ferrofluid magnetization theory properly taking account of interparticle interactions is the objective of many theoretical works. This topic has been discussed for at least 20 years (e.g. in [26], [27], [29], [30], [31], [32], and [33]). In the course of time, different models were proposed; each of them more or less valid in different concentration and temperature ranges.

Validity check: Vicious circle of polydispersity

Comparison with experiments enables to check a magnetization theory for validity. But for meaningful comparison, the theory must incorporate the *same* $p(d)$ as used in the experiments. Otherwise, interparticle interaction effects are *hidden* behind a *wrong* magnetic core diameter distribution and a safe statement about the theorie's validity is not possible. Hence, $p(d)$ of the ferrofluid used in the experiments must be known as good as possible. As stated in part 3.1.2, *magnetic* core size information can only be obtained by magnetization measurements. In particular, by a so-called *magneto-granulometric analysis* (**MGA**). In anticipation of the more detailed introduction in the next part, MGA *requires an exact magnetization theory* to deliver precise information about $p(d)$. This sounds very adverse, but nevertheless there is a loophole from this vicious circle, allowing the validation of a magnetization theory, as will be explained right after the introduction of MGA.

Magneto-granulometric analysis

Two of the first papers introducing MGA in the 1970's were [23] and [34]. The basic idea is to extract two characteristical quantities – like e.g. M_∞ and χ_{init} – from the experimentally gained magnetization curve of a ferrofluid. A magnetization theory then provides relations between the measured quantities and the n-th moment $\langle m^n \rangle$ of the ferrofluid's magnetic moment distribution: $M_\infty(\langle m \rangle)$ and $\chi_{init}(\langle m^2 \rangle)$ in case of the example above. Measurement and theory in combination would then provide $\langle m \rangle$ and $\langle m^2 \rangle$, yielding two moments of $p(d)$; $\langle d^3 \rangle$ and $\langle d^6 \rangle$. Assuming a two-parametrical distribution function $p(d)$ like the lognormal or gamma distribution (part 3.1.2), these two moments define both parameters (via Equations 3.5 and 3.10, respectively).

Obviously, the validity of the MGA result is not easy to assure. It depends on

- the precision of the experiment,
- how well the theory describes reality,
- and validity of the assumed distribution function.

In spite of all the uncertainties named above, MGA is a convenient tool to check if a magnetization theory M_{theo} correctly includes the particle density effect. Consider the following experiment:

A *very dense* ferrofluid is split up in several samples. Each of them is being diluted to a certain degree, resulting in ferrofluid samples

- covering a huge range of particle concentration
- and all having the *same* magnetic core diameter distribution $p(d)$.

An MGA upon all the samples using M_{theo} **must** result in the **same** distribution parameters for **each** of the samples, if M_{theo} is **correctly** incorporating the density effect [27].

3.2.3 Second-order modified mean-field theory

Over the time, several authors developed a whole bunch of different models taking account of interparticle interactions. In [33], a publication from 2007, six important theories have been tested for validity

via MGA and via comparison with molecular dynamics / monte carlo simulations. The only theory fulfilling the "MGA-criterion" (as described above: same $p(d)$ data for all concentrations) is the so-called *second-order modified mean-field theory* (**MMF2**), which was initially presented in [32] (2001).

The authors performed a rigorous analysis of the two and three-particle correlation functions in dipolar fluids incorporating the dipole-dipole interaction energy and were able to – among others – generate an expression for the effective field H_e properly representing their model in terms of the SPM:

$$M_{MMF2}(H,\rho) = M_{SPM}(H_e(H,\rho),\rho) \tag{3.14}$$

$$\text{with } H_e = H + \frac{1}{3}M_{SPM}(H)\left(1 + \frac{1}{48}\frac{dM_{SPM}(H)}{dH}\right) \tag{3.15}$$

Expanding this using Equation 2.18 clearly shows that the MMF2 magnetization is **non-linearly** dependent on ρ:

$$M_{MMF2}(H,\rho) = \rho M_s \left\langle \mathcal{L}\left(\frac{\mu_0 m(d) H_e}{kT}\right)\right\rangle \tag{3.16}$$

$$H_e(H,\rho) = H + \frac{1}{3}M_s\rho\left\langle \mathcal{L}\left(\frac{\mu_0 m(d) H}{kT}\right)\right\rangle \cdot\left(1 + \frac{1}{48}M_s\rho\frac{d}{dH}\left\langle \mathcal{L}\left(\frac{\mu_0 m(d) H}{kT}\right)\right\rangle\right)$$

Terms of the order ρ and ρ^2 appear *within* the LANGEVIN function.

As stated in [32], MMF2 very accurately describes the total magnetization curve of dense ferrofluids (up to $\sim 18\,\%$ magnetic phase fraction of the total volume). This was verified in [33], stating that MMF2 is a theory with very good overall reliability, applicable in quite wide concentration and temperature ranges.

Chapter 4

Signal characterization by simulation

This chapter is about the investigation of the impact of particle size and density on MPS/MPI via numerical simulations, based on considerations and theory introduced in chapters 2 and 3.

4.1 Simulation methods

All simulations were accomplished using either MATLAB (a numerical computing environment by THE MATHWORKS) or MATHEMATICA (a computer algebra system by WOLFRAM RESEARCH). Regarding MPI, both have their advantages.

MATLAB allows for easy implementation of the vector characteristics of the magnetic field configuration, needs short source code and can perform as well as machine-oriented code. In MATHEMATICA, numerical noise can be reduced as much as desired by using *arbitrary-precision arithmetics* at the cost of performance. This can be useful, because the higher harmonic amplitudes in MPI have a very high *dynamic range*, which can collide with MATLAB's double precision: it quickly happens that numerical noise dominates and breaks an MPI simulation implemented in MATLAB[1].

[1] In particular in case of noise amplification due to the "iω-method" (cf. Equation 2.41), which linearly intensifies the noise of the result of a discrete FOURIER

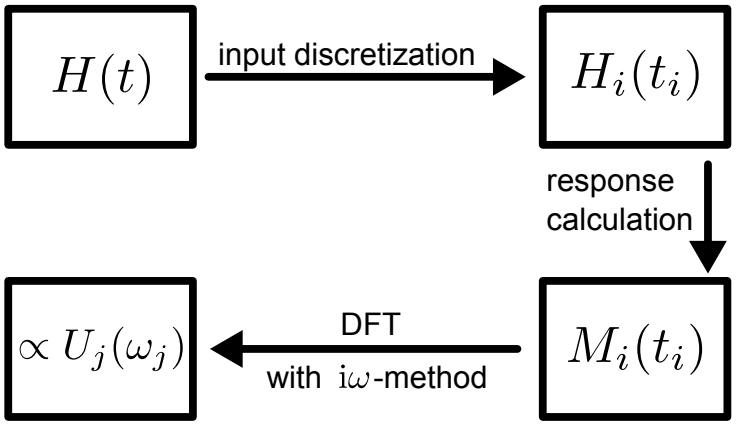

Figure 4.1: Flowchart of the execution performed within each MPI/MPS signal simulation: after formal definition of the input signal $H(t)$, it is discretized to the vector $H_i(t_i)$, which is put into a magnetization theory $M(H)$, yielding the response $M_i(t_i)$. $\mathrm{DFT}(M_i(t_i))$ and multiplication with $\mathrm{i}\omega$ (cf. Equation 2.41) provides a discrete spectrum proportional to the frequency spectrum $U_j(\omega_j)$ of the detectable output voltage.

4.1.1 Proper signal sampling and DFT in Matlab/Mathematica

Core components of each MPS/MPI signal simulation are *discrete* input signal creation, response building and discrete FOURIER transformation (DFT), as visualized in Figure 4.1. The input sampling parameters during the "input discretization step" have to be chosen very carefully, because they define the discretization characteristics of $M_i(t_i)$, which is the DFT *input vector*. It specifies the complexity of the DFT and the quality of its result and – with that – the duration and goodness of the simulation of the amplitudes of the higher harmonics. Understanding the *output vector* of DFT is complex, too: value interpretation, normalization, and frequency assignment require understanding and care. Helpful literature are the articles [35] and [36].

The following parts discuss optimal sampling and DFT output interpretation methods for MPI and show short FOURIER analysis examples in MATLAB and MATHEMATICA based on these methods.

transformation (DFT) with increasing frequency.

DFT input: optimal sampling method

A discretization/sampling method is entirely defined by t_i, the set of points in time at which the input signal is sampled. It turns out that the t_i of an *optimal* DFT input vector for MPI/MPS simulations are the following ones:

$$t_i = 0, \Delta t, 2\Delta t, \ldots, T - \Delta t \tag{4.1}$$

with $T = 2\pi/\omega_0 = 1/f_0$ being the period of the sampled input signal and Δt being the sampling interval fulfilling

$$\Delta t = \frac{T}{m} \quad \text{with} \quad m \in \mathbb{N}. \tag{4.2}$$

A DFT calculates the spectrum of the *infinite periodic continuation* of the input. With prior knowledge of the input signal's periodicity T, **the so-called *leakage effect* can be eliminated by *perfect* DFT *windowing*[1], which is realized via Equation 4.1.**

The output vector of a DFT always is as long as its input dataset: the number of data points in both, input and output, is N. The sampling frequency $f_s = 1/\Delta t$ together with N defines the frequency resolution Δf of the DFT (the frequency distance between two neighboring output data points) and the highest reliably detectable frequency f_{limit}:

$$\Delta f = \frac{f_s}{N} \quad \text{and} \quad f_{limit} = \frac{f_s}{2} - \Delta f \tag{4.3}$$

The special sampling method as given by Equation 4.1 only analyzes *one* period. This leads to $N = m$ and, hence, Δf being independent on the sampling frequency:

$$\Delta f = \frac{f_s}{N} = \frac{m}{NT} = \frac{1}{T} = f_0 \tag{4.4}$$

[1] Signal sampling is limited to a finite interval of time, which is equivalent to applying a rectangular so-called window function to the real signal. Consider a T-periodic signal. If the window length L is not exactly $L = nT - \Delta t$ (with Δt being the sampling interval and $n \in \mathbb{N}$), the *infinite periodic continuation* of the gathered data does not match the real signal. Instead, sudden discontinuities are introduced. In a DFT's output they manifest themselves in high frequency terms not occurring in the real signal, and too low real frequency contributions ("leakage effect" [37]).

Thus, the discussed sampling method can (only) detect contributions with frequencies

$$0,\ f_0,\ 2f_0,\ \ldots,\ n_{max}f_0 \tag{4.5}$$

with n_{max} being the nearest integer less than or equal to $m/2-1$, as given by f_{limit}. MPI theory forces all other (non higher harmonic) contributions to be zero, so the sampling method given by Equation 4.1 uses the *smallest data set possible* to obtain a specific amount of information. Therefore, **the method has maximum performance.**

DFT output: interpretation

For DFT output analysis, at first the data points itself have to be assigned to *frequencies*: the first output data point with index 1 belongs to frequency 0, the increment is Δf (as given by Equation 4.3) and the last data point with index N belongs to $f_{sample}-\Delta f$.

The entire output data set contains redundant information: each value is a complex number c, containing information about the a_n and b_n of Equation 2.27. All information gained by DFT can be found from index 1 to the nearest integer less than or equal to $N/2+1$; other values with higher indices are complex conjugates of values from the first half, so they do not contain new information.

Interpretation of the data *values* is generally quite complex. But, assuming the input signal with fundamental frequency $1/T=f_0$ to be perfectly sampled as described above and assuming all contributing oscillations starting with the *same phase*, makes interpretation very easy: consideration of $|c|$ together with proper normalization then yields a correct FOURIER analysis, providing the amplitudes A_n of the higher harmonics with frequency nf_0.

The "proper normalization" depends on the actual DFT implementation. Commonly, the data has to be divided by N and multiplication with 2 does justice to the fact that amplitudes are split up evenly between the first and the second half of the output of the DFT[1].

[1] For correct determination of an offset (at frequency 0), the first data point of the output must not be doubled, because it does not have a symmetric counterpart.

DFT in Matlab: minimal example

MATLAB's actual DFT implementation is provided by the function $\mathrm{fft}()$, based on the so-called "Fastest Fourier Transform in the West" (FFTW) [38] and exhibits the complexity $\mathcal{O}(N \log N)$. Up next, there is a minimal example how to use and wrap this function to perform a proper FOURIER analysis of the signal

$$a(t) = 2\sin(\omega_0 t) + \sin(2\omega_0 t) + 5\sin(3\omega_0 t);\ f_0 = \frac{\omega_0}{2\pi} = 1, \quad (4.6)$$

based on the considerations made above:

- Define sampling constants for realization of the sampling method given by Equation 4.1:

```
f_0 = 1;            % fundamental frequency
f_sample = f_0*8;   % sampling frequency
L = 1/f_0;          % length of sampled signal: 1 period
dt = 1/f_sample;    % sampling interval
t = (0:dt:L-dt);    % vector containing the sample times
N = length(t);      % length of DFT input and output
df = f_sample/N;    % freq step between two output points
```

- Build frequency vector for output interpretation:

```
freqs = (0:df:f_sample-df);
```

- Sample signal (build DFT input vector $a_i(t_i)$):

```
w_0 = 2*pi*f_0;
A = 2*sin(w_0*t) + sin(2*w_0*t) + 5*sin(3*w_0*t);
```

- Accomplish normalized DFT (as described above):

```
freq_spectrum_A = 2*abs(fft(A))/N;
```

- Examine amplitude-frequency-pairs for relevant part of output:

```
freq_spectrum_A(1:floor(N/2+1))
freqs(1:floor(N/2+1))

ans = 0.0000    2.0000    1.0000    5.0000    0.0000
ans = 0         1         2         3         4
```

Hence, the A_1, A_2, A_3 of the higher harmonics of signal $a(t)$ were correctly computed (limited by MATLAB's internal precision). Implementation of the "iω-method" (cf. Equation 2.41) to determine the amplitudes of the higher harmonics of $\frac{d}{dt}a(t)$ is as follows:

- Multiply each DFT output data point with iω; examine output:

```
freq_spectrum_dt_A = 2*abs(1i*2*pi*freqs.*fft(A))/N;
freq_spectrum_dt_A(1:floor(N/2+1))
freqs(1:floor(N/2+1))

ans = 0   12.5664   12.5664   94.2478    0.0000
ans = 0   1         2         3          4
```

These values correspond to the analytical results of the amplitudes of the higher harmonics of $\frac{d}{dt}a(t)$: $A_1 = A_2 = 4\pi$, $A_3 = 30\pi$.

DFT in Mathematica: minimal example

Now, the same signal $a(t)$ (Equation 4.6) is analyzed using MATHEMATICA. Here, the DFT is provided by the Fourier[] function. Without knowing details about the internals, it is exhibiting the same complexity as MATLAB's fft() function ($\mathcal{O}(N \log N)$).

The implementation of the analysis is completely analogous to the one in MATLAB, but features arbitrary-precision calculation:

- Define sampling constants and build frequency vector (*exact*):

```
f0 = 1;
fsample = f0*8;
L = 1/f0;
dt = 1/fsample;
t = Table[t,{t,0,L-dt,dt}];
n = Length[t];
df = fsample/n;
freqs = Table[f,{f,0,fsample-df,df}];
```

- Sample signal (values are stored in *exact* form); accomplish normalized[1] DFT (output is calculated in *200-digit precision*):

```
w0=2*Pi*f0;
A[time_] = 2*Sin[w0*time]+Sin[2*w0*time]+5*Sin[3*w0*time];
Asamples = Map[A,t];
Aspectrum = 2*Abs[Fourier[N[Asamples,200],
                          FourierParameters->{1,-1}
                         ]
                  ]/n;
```

- Examine amplitude-frequency-pairs[2]:

```
Part[N[Chop[Aspectrum,10^-190],4],1;;Floor[n/2+1]]
Part[N[freqs,4],1;;Floor[n/2+1]]

{0, 2.000, 1.000, 5.000, 0}
{0, 1.000, 2.000, 3.000, 4.000}
```

- Calculate and examine spectrum of $\frac{d}{dt}a(t)$:

```
dtAspectrum = 2*Abs[I*2*Pi*freqs*
                    Fourier[N[Asamples,200],
                            FourierParameters->{1,-1}
                           ]
                   ]/n;
Part[N[Chop[dtAspectrum,10^-190],6],1;;Floor[n/2+1]]
Part[freqs,1;;Floor[n/2+1]]

{0, 12.5664, 12.5664, 94.2478, 0}
{0, 1,       2,       3,       4}
```

Like in the MATLAB example, all results are as analytically expected. Additionally, the numerical precision of the result can be chosen as required for further processing. But this decreases the computing performance: In a benchmarking test[3], 100 independent runs of sampling (100000 data points), DFT and "iω-method" in MATHEMATICA took 840 s (with 200-digit precision, and 750 s with 50-digit precision),

[1] The specific $\mathrm{FourierParameters}$ setting allows for division by N for proper normalization (hence, it creates same behavior as in MATLAB).

[2] Every output data value smaller than 10^{-190} is considered as 0.

[3] Using one core of an INTEL P8800 CPU (2.66 GHz) and 4 GB random access memory.

while MATLAB approximately needed $1.3\,\mathrm{s}$ (IEEE double-precision [39]: 52 bit / 10^{-16}).

4.2 Magnetic Particle Spectroscopy

4.2.1 Impact of magnetic core diameter

The qualitative discussion in part 3.1.1 revealed that the amplitudes A_n of the higher harmonics in MPS/MPI heavily depend on the magnetic core diameter d of the particles. This relation was investigated quantitatively via several MPS simulations using different magnetic core diameters.

As stated in 2.5.2 ("Ferrofluid magnetization response – Fourier analysis of the MPS signal"), the A_n seem to decay almost exponentially for higher n. Consequently, in each simulation with a specific d, the decay of A_n with increasing n can be fit to the model

$$A_n = C\mathrm{e}^{-kn}. \tag{4.7}$$

The objective is to investigate the relation between the diameter d and the strength exponential decay of the higher harmonics, as given by the fit parameter k. Therefore, many simulations with changing d have been performed, leading to $k(d)$.

95 different diameters between $d_{min} = 2.5\,\mathrm{nm}$ and $d_{max} = 50\,\mathrm{nm}$ were simulated. Within each of the simulations, the exciting magnetic field has an amplitude of $5\,\mathrm{mT}$. The "ferrofluid sample" is considered to consist of monodisperse magnetite particles, with their magnetic moment given by $m(d)$ (Equation 2.14). The sample's response analyzed spectroscopically is the *relative* magnetization as given by the SPM. Hence, total amount of substance and density effects are masked out and comparison of different responses for different d exhibits the pure impact of d on the A_n. For each d, Equation 4.7 has been fitted to the A_n for $n = 3, 5, \ldots, 13$.

Figure 4.2 shows two example fits, visualizing maximum and minimum agreement of data and model between d_{min} and d_{max}: the fit for $d = 5\,\mathrm{nm}$ agrees very well with the exponential model; the agreement of the fit for $d = 32\,\mathrm{nm}$ is still acceptable. Thus, evaluation of $k(d)$ is justified.

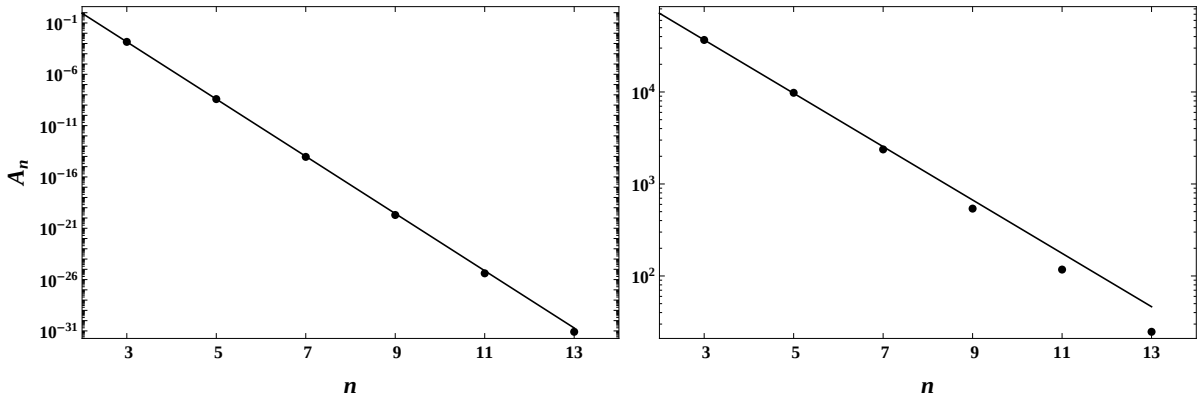

Figure 4.2: Dots: n-th higher harmonic amplitude A_n, obtained by simulation of the relative magnetization of a ferrofluid (particle core material: magnetite; magnetic core diameter d: 5 nm (left) and 32 nm (right); excitation field amplitude: 5 mT). Solid lines: Exponential fits based on Equation 4.7. From many fits for $2.5\,\text{nm} \leq d \leq 50\,\text{nm}$ the left graph shows one of the best and the right one shows one of the worst fits.

Figure 4.3 shows the result of the simulation: for constant environmental conditions[1], the strength of the exponential decay seems to depend on d exponentially itself. Thus, **signal optimization (intensification) by particle size enlargement definitely does make sense** in a range where $k(d)$ rapidly changes with d (below $d \approx 15\,\text{nm}$ in this case). For larger d, a trade-off is required between small signal enhancements and a potentially large effort related to further particle enlargement.

The source code of the simulation can be found in Appendix A.2 (page 101).

4.2.2 Impact of particle concentration

This section is about the investigation of the dependency of MPS on the concentration of magnetic particles. These investigations are based on the MMF2 theory, as introduced in part 3.2.3.

[1] In particular for constant excitation field amplitude, which certainly has a considerable impact at this point.

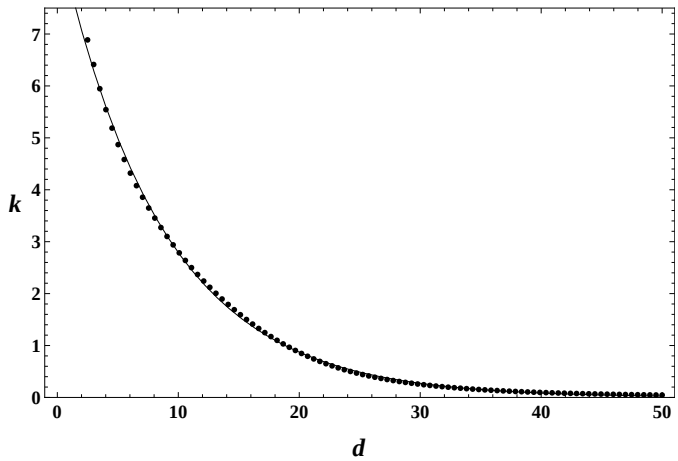

Figure 4.3: Points: Strength k of the exponential decay of the A_n (cf. Equation 4.7) in dependence of magnetic core diameter d (obtained by MPS simulations with constant experimental setting). Line: Exponential fit of the data points.

Density-concentration conversion

Throughout the thesis, the terms "particle density" and "particle concentration" were used as synonyms. But there is a useful distinction: the density ρ (as used in magnetization theory formulas for the SPM (2.18) and MMF2 (3.16)) denotes the magnetic phase fraction of the total volume and therefore is defined between 0 and 1 (with unit 1), with 1 corresponding to the bulk material. The concentration c however specifies the amount of magnetic substance per volume in mol/l. While ρ is useful in theoretical works, declaration of concentrations in mol/l is well-established in papers regarding real applications of magnetic particles. Therefore, simulation results are given in dependence of c, while internal calculations are done using ρ.

Conversion from c to ρ and the other way round can be done easily by knowledge of the *molar volume* V_{mol} of the considered substance:

$$c(\rho) = 10^{-3}\frac{\rho}{V_{mol}} \tag{4.8}$$

V_{mol} is calculated from the density (mass per volume) and molar mass of the substance. The molar mass is obtained by multiplying the AVOGADRO constant with the molecular/atomic mass of the substance (as

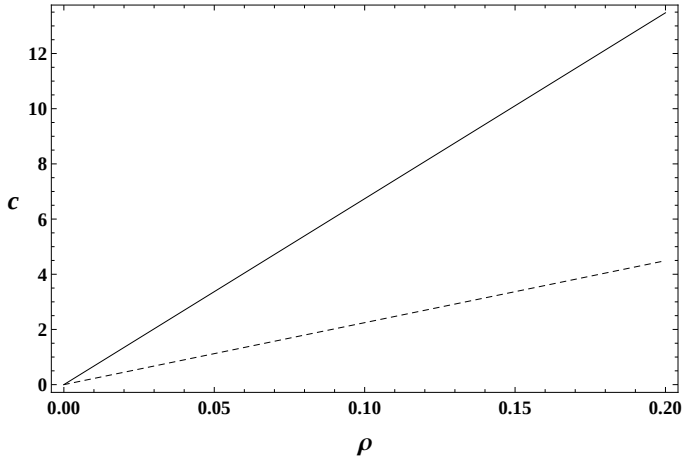

Figure 4.4: Conversion of particle density ρ [1] into concentration c [mol/l], as given by magnetite's density (mass per volume) and molar volume. Solid line: Iron concentration. Dashed line: magnetite concentration.

given by a periodic table). For magnetite (Fe_3O_4, density $5.2\,\mathrm{g/cm^3}$ [40]), this results in

$$V_{mol,magnetite} = 44.5 \cdot 10^{-6} \frac{\mathrm{m}^3}{\mathrm{mol}}. \tag{4.9}$$

Even if the magnetic core material used in an experiment is magnetite, people mostly are interested in the *iron* concentration c_{Fe}, which is 3 times $c_{\mathrm{Fe_3O_4}}$.

For being able to classify a given c or ρ, their relation is visualized in Figure 4.4. The range of ρ presented corresponds to the scope of validity of MMF2.

Global concentration vs. local concentration

Concentration or density is always *per volume*. For investigation of the concentration effect, the size of the volume considered to *define* a concentration has to be clear. There, two types of definitions have to be separated carefully: the "global concentration" and the "local concentration".

In the magnetization formulas 2.18 and 3.16, the term ρM_s gives the saturation magnetization M_∞ of the ferrofluid, corresponding to

the absolute amount of magnetic substance within **the total volume of the sample**. So, there, ρ is the *global* (or mean) particle density. Only in the special case of a *homogeneously* mixed ferrofluid, the global concentration is the same as the *local* concentration within each conceivable **sub-volume containing at least a few particles**. This case is considered by the magnetization theories. Therefore, the *total* magnetization as given by the SPM linearly depends on ρ, which is proportional to the total amount of magnetic substance and – with that – to M_∞.

In reality, the *local* particle density may fluctuate within the considered volume; which is without consequence when calculating M_∞. The effect of *local* particle concentration fluctuations on the magnetization of the whole sample is investigated in this part.

For investigation of this effect by simulation, *relative* magnetizations are analyzed, so that the considered total volume of the sample is of arbitrary size, leading to c or ρ always denoting a *local* concentration. Evaluation of the relative magnetization as given by the SPM or MMF2 is equivalent to analyzing ferrofluids with homogeneously distributed particles and with a constant total amount of magnetic substance (i.e. shrinking the ferrofluid volume while increasing its concentration).

Impact of local concentration on MMF2 magnetization curve

Plotting the *relative* magnetization curve of a monodisperse ferrofluid as given by MMF2 for different particle concentrations visualizes the *pure* local concentration effect. This was accomplished in MATLAB, using the MMF2 implementation shown in Appendix B.1 (page 108).

The result is presented in Figure 4.5. MMF2 exhibits an increasing initial susceptibility χ_{init} with increasing c, as qualitatively predicted in 3.2.1. Therefore, curvature (non-linearity) strongly depends on c. How this impacts MPS is analyzed quantitatively in the next part.

The graph shows the convergence of MMF2 to SPM for $c \to 0$. Furthermore, it allows for an estimation of the error of the SPM with increasing c.

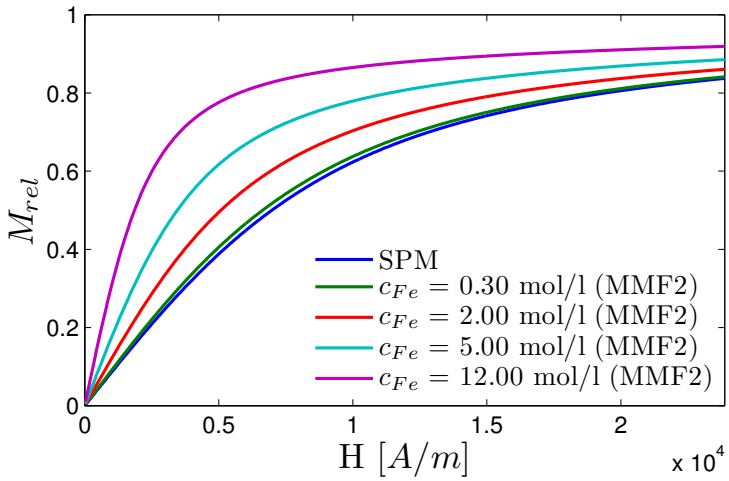

Figure 4.5: Relative magnetization of a monodisperse ferrofluid (made of magnetite particles with magnetic core diameter $d = 15$ nm), as given by MMF2 (Equation 3.16) for different *local* particle densities translated to local iron concentrations c_{Fe} (cf. Equation 4.8). The range of H shown corresponds to 0 to 0.03 T.

Effective particle diameter (and cluster particles)

As explained in part 3.2.1 ("Impact of interparticle coupling"), the change of the magnetization curve due to the local concentration effect is qualitatively similar as due the change to enlargement of the magnetic core diameter. This was investigated quantitatively by fitting the SPM magnetization curve to the MMF2 curve for a given *real* particle diameter and (high) density, using not the real, but an *effective* diameter d_{eff} within the SPM as fit parameter. This procedure is visualized in Figure 4.6.

The concentration used within the MMF2 calculation is $c_{Fe} = 12$ mol/l. While it is unlikely to find a ferrofluid with such a high global concentration, 12 mol/l or much more are conceivable in very localized environments, e.g. in particle *clusters*, consisting of many small particles which are forming an object that – viewed from some distance – has the same magnetic properties as a single magnetic particle with an effective diameter d_{eff}.

The magnetic core diameter within the MMF2 calculation – which

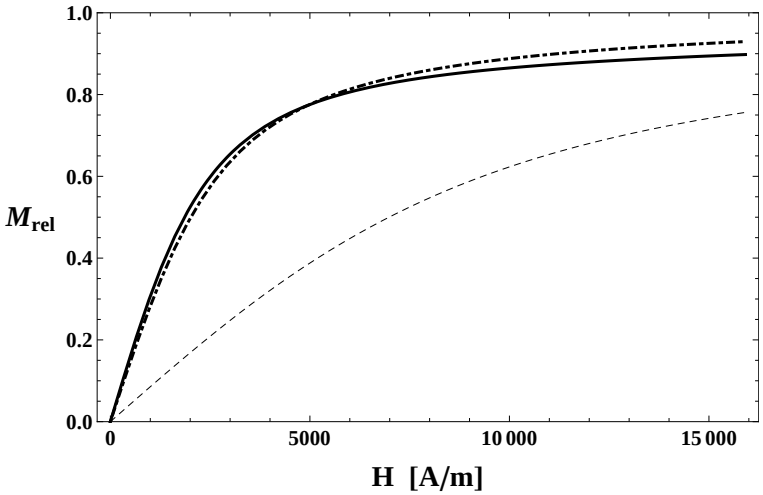

Figure 4.6: Solid line: relative magnetization curve $M_{rel}(H)$ for $d = 15\,\text{nm}$ and $c_{Fe} = 12\,\text{mol/l}$, given by MMF2. Dashed line: $M_{rel}(H)$ as given by SPM for $d = 15\,\text{nm}$. Dotdashed line: $M_{rel}(H)$ given by SPM for $d_{eff} = 22.7\,\text{nm}$ (effective diameter, minimizing the integral over the squared difference between SPM and MMF2 magnetization curve).

can be considered as the *real* diameter – was chosen to be $15\,\text{nm}$. In contrast, the dotdashed line in Figure 4.6 is the SPM curve for $d_{eff} = 22.7\,\text{nm}$. It minimizes the squared difference[1] between the SPM and MMF2 magnetization curves, integrated over the *relevant* magnetic field range (in this case, this is the range shown in the plot).

The MATHEMATICA source implementing this calculation is shown in Appendix A.3 (page 104).

As can be seen in the initial MPI publication [1], this effect can have very severe consequences:

> "*Given that the particles have a reported diameter of* $4\,\text{nm}$*, [...]. [...] The experimental data fit well, assuming that particles of* $30\,\text{nm}$ *diameter are responsible for the signal.*"

[1] The effective diameter d_{eff} as defined here depends on the fitting method. The "method of least squares" was chosen, because it is the standard approach for curve/data fitting. It effectively prevents big differences in a few places, but allows for very small differences everywhere.

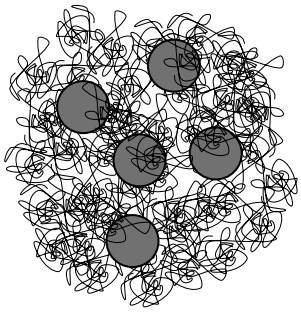

Figure 4.7: Schematic picture of a cluster particle containing many small magnetic cores, tightly packed within a polymer shell.

The authors used Resovist[1], which consists of *clustered* particles: each of them is made of many small particles ($3 - 5$ nm diameter). These are *tightly* packed in a dextran shell, resulting in a hydrodynamic diameter of about 60 nm [41], as illustrated in Figure 4.7. Regarding this extremely high local particle concentration, it is clear that the effective particle diameter of RESOVIST vastly deviates from the diameter of a single core. In 2009, another group analyzing the MPS signal of RESOVIST reported an effective particle diameter of about 15 nm [24] without further explanation.

Impact of local particle concentration on MPS

To investigate the pure impact of local concentration on the higher harmonic amplitudes A_n in MPS, the best choice is to simulate the *relative* magnetization response of a *monodisperse* ferrofluid, so that total amount of substance and particle diameter effects are masked out. Based on MMF2, this was accomplished with MATLAB for the harmonics 3 to 9 of a ferrofluid containing particles with $d = 15$ nm, getting excited due to an irradiated field with 5 mT amplitude. For comparison, the simulation was done using the SPM, too.

The result of the simulation is shown in Figure 4.8. As expected – due to the paramagnetic nature of the SPM – the A_n simulated via SPM do not depend on local concentration changes. In contrast, the

[1] A commercially available contrast agent made of magnetite SPIOs. See [41] for details.

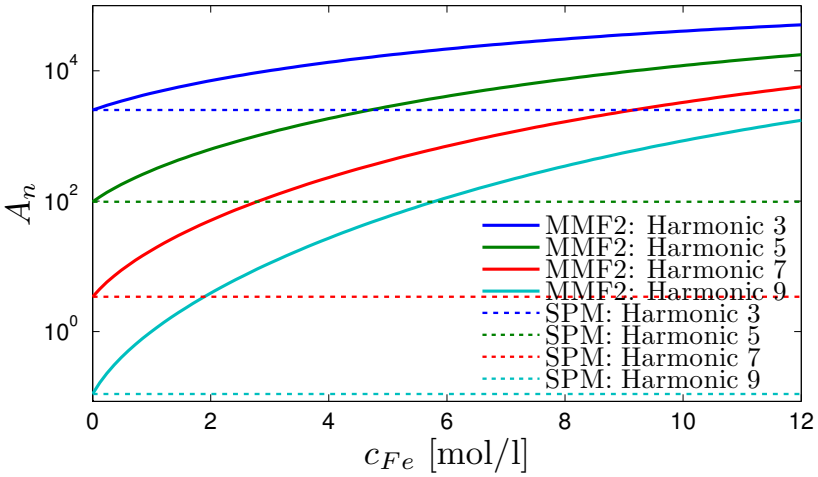

Figure 4.8: n-th higher harmonic amplitude A_n in dependence on local iron concentration c_{Fe}, obtained by simulation of the *relative* magnetization response of a ferrofluid based on MMF2. Simulation performed for $d = 15$ nm and 5 mT excitation field amplitude.

incorporation of particle coupling effects by means of MMF2 leads to a drastic enhancement of A_n with increasing c. The enhancement per Δc grows with n, i.e. higher harmonics with larger n are affected more. The total amplitude enhancement can span orders of magnitude for (considerably) high c.

Since MMF2 theory provides realistic results, the graph shows that **the unmodified SPM**[1] **is *inapplicable* for predicting higher harmonic amplitudes in case of moderate and high local particle concentrations.** In biological applications, local particle densities significantly exceeding the scope of validity of the SPM will not be uncommon. A prime example – leading to iron concentrations of $0.2 - 5$ mol/l – is the agglomeration of magnetic particles in cells [42].

In terms of the SPM, the A_n can only vary due changes in the total amount of magnetic substance, which can be modeled by a constant factor *each* A_n gets multiplied with[2]. Therefore, the ratio of different

[1] Using the real particle diameter.

[2] This effect can not be seen when simulating the relative magnetization, which is independent on total amount of substance changes.

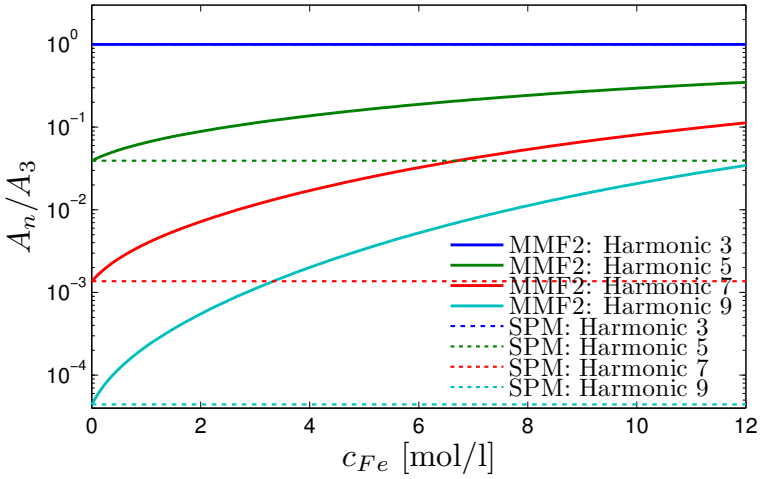

Figure 4.9: n-th higher harmonic amplitude A_n normalized to A_3 in dependence on local iron concentration c_{Fe}, obtained by simulation of a ferrofluid's *relative* magnetization response based on MMF2. Simulation performed for $d = 15$ nm and 5 mT excitation field amplitude.

A_n is *always constant*. **A very important characteristic introduced by interparticle coupling is that the ratio of two A_n changes with varying particle concentration.** This effect is visualized in Figure 4.9, showing the harmonics 3 to 9 again, but this time normalized to A_3.

The ratio of the 3rd and the 5th/7th/9th amplitude drastically changes with increasing concentration. In general, the MMF2 curves "move together" with rising c_{Fe} (this is observable in Figure 4.8, too), leading to the conclusion: **the higher n, the larger the amplitude change ΔA_n due to the same local particle concentration change Δc.** This again shows the similarity of the impact of local particle concentration and of particle diameter: it means that the exponential decay strength of A_n (to higher n) decreases with rising local particle concentration. As shown in 4.2.1, an increasing magnetic core diameter qualitatively *has the same effect.*

This behavior is very useful for detecting changes of the local particle concentration in an experiment: if the ratio of two amplitudes A_{n_1}/A_{n_2} significantly differs between two measurements of the same ferrofluid, the local particle concentration must have changed. This fact is verified experimentally in 5.1.2. Furthermore, the relation

can be used for a practical application, as described in chapter 6.

4.3 Magnetic Particle Imaging

4.3.1 Offset field parallel / perpendicular

As brought up in 2.5.2 ("Ferrofluid magnetization response – Excitation: magnetic field irradiation"), non-parallel alignment of the offset field $\vec{H}_{off}$ and excitation field $\vec{H}_{exc}$ may exhibit advantages for MPI. The angle between the fields is an additional degree of freedom introducing new physical aspects. One aspect is to avoid potentially disturbing π phase jumps in the point spread function (PSF) of conventional MPI ($\vec{H}_{off} \parallel \vec{H}_{exc}$) using perpendicular alignment: $\vec{H}_{off} \perp \vec{H}_{exc}$, as proposed in [18]. This was examined by means of simulation.

The dependence of a specific higher harmonic amplitude A_n on the offset field strength $|\vec{H}_{off}|$ is leading to a PSF of certain shape for this specific harmonic, considering the spatial dependency of the offset field. This can be explained using the frequency mixing method (2.6.2): The excitation $\vec{H}_{exc}(t) = \vec{H}_{exc}\sin(\omega_0 t)$ can be taken into consideration separately from the spatially dependent offset field $\vec{H}_{off}(\vec{x})$. The n-th higher harmonic resulting from the excitation varies with the offset field strength (cf. 2.6.1), leading to $A_n(|\vec{H}_{off}|)$. Together with $\vec{H}_{off}(\vec{x})$[1], this dependency defines the PSF of the n-th harmonic.

In the simulation, $A_3(|\vec{H}_{off}|)$ was compared for the parallel case $\vec{H}_{off} \parallel \vec{H}_{exc}$ and the perpendicular case $\vec{H}_{off} \perp \vec{H}_{exc}$. The *parallel* case is

$$\vec{H}_{exc}(t) = \begin{pmatrix} 0 \\ 0 \\ H_{exc_z} \end{pmatrix} \sin(\omega_0 t) \quad \text{and} \quad \vec{H}_{off} = \begin{pmatrix} 0 \\ 0 \\ H_{off_z} \end{pmatrix}. \tag{4.10}$$

The *perpendicular* case is

$$\vec{H}_{exc}(t) = \begin{pmatrix} 0 \\ 0 \\ H_{exc_z} \end{pmatrix} \sin(\omega_0 t) \quad \text{and} \quad \vec{H}_{off} = \begin{pmatrix} 0 \\ H_{off_y} \\ 0 \end{pmatrix}. \tag{4.11}$$

[1] The actual relation between $\vec{H}_{off}$ and $\vec{x}$ does not matter here, but can be imagined as constant field gradient in a certain direction.

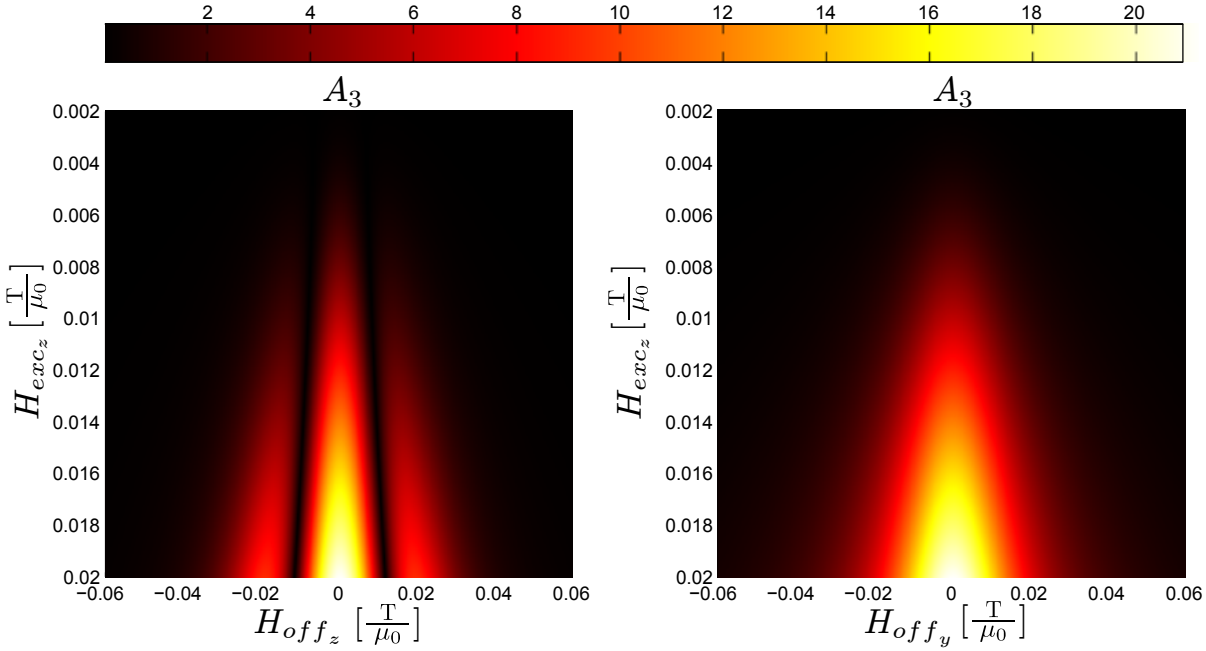

Figure 4.10: Left: Third higher harmonic amplitude A_3 (encoded by color) in dependence of *parallelly* aligned offset field $\vec{H}_{off}$ and excitation field $\vec{H}_{exc}$. Right: A_3 in dependence of *perpendicularly* aligned $\vec{H}_{off}$ and $\vec{H}_{exc}$.

The magnetization response is detected in direction of excitation (z-direction).

In both cases, $A_3(H_{exc_z}, |\vec{H}_{off}|)$ was analyzed for 400 different excitation field amplitudes (between 2 and 20 mT) and 400 offset field strengths (between -60 and 60 mT), using the relative SPM magnetization for magnetite particles ($d = 15$ nm).

The result, which is visualized in Figure 4.10, shows distinct differences between the two cases. For fixed H_{exc_z}, A_3 has roots along the H_{off_z} direction (parallel alignment). They do not occur for perpendicular alignment. Actually, by going through a root of the *amplitude*, a phase jump of π takes place, as revealed by evaluation of the amplitude *and* phase of the DFT result. Hence, as given by $\vec{H}_{off}(\vec{x})$, it is possible that signal emission of two different locations happens with equal amplitudes and a π phase shift. Simultaneous detection then yields destructive interference, resulting in signal cancellation or at

least damping. It is conceivable – but has to be investigated – that this effect plays a considerable role in real MPI applications.

As a matter of fact, in the parallel case *all* higher harmonics A_n exhibit one or more π phase jumps with changing $|\vec{H}_{off}|$. This never occurs in the perpendicular case, so that destructive interference is not a problem here. But the perpendicular configuration has disadvantages or at least particularities, too. Due to preserved magnetization symmetry in detection direction, *only odd harmonics occur*. From a theoretical point of view, this should not restrict imaging capabilities in comparison with the parallel case.

A disadvantage of the perpendicular case is that the decay of the PSF to high offset field strengths is *weaker* than in the parallel case, so that the PSF as a whole is wider (considering the same excitation field strength).

The core components of the MATLAB code creating the data shown here can be found in Appendix B.2 (page 109). The code is optimized for high performance vector calculations; it processes arbitrarily aligned vectors $\vec{H}_{off}$ and $\vec{H}_{exc}$.

4.3.2 Linear reconstruction method vs. non-linear concentration dependency

In 3.2, the non-linear dependence of the magnetization curve on particle concentration was predicted qualitatively. MMF2 was introduced as a theory incorporating this effect very well. As shown in 4.2.2, a (considerably) high particle concentration has huge impact on the higher harmonic amplitudes in MPS/MPI. It was shown that a magnetization model which is linear in ρ (SPM) is not suitable for predicting these.

The intention of this part is to examine the impact of the non-linear concentration dependency on MPI. Therefore, 1D MPI using the drive field method (DFM, as described in detail in part 2.6.3) was implemented. The properties of the simulation are described within the next paragraphs.

1D phantom

The phantom used within the simulation is the 1D ferrofluid concentration distribution $c_{Fe_3O_4}(x)$ (magnetite, $d = 15\,\text{nm}$). It is chosen to

exhibit $c_{Fe_3O_4} = 1$ [mol/l] at some points (which is a moderately high concentration) and $c_{Fe_3O_4} = 0$ everywhere else. For simulation, the phantom is discretized to 200 pixels with the locations x_i. $x = 0$ is defined to be the center of the phantom; its total length is defined as L. The phantom is visualized in the top graph of Figure 4.11.

Magnetic field configuration

To gain a signal within the framework of the drive field method, a magnetic field gradient has to be "driven over the phantom" (as described in 2.6.3 and indicated in Figure 2.9). This is realized by the field

$$H(x,t) = G(x) - H_{drive}\sin(\omega_{drive}t). \tag{4.12}$$

The gradient G is chosen to $1\,\mathrm{T}/L$. The drive field amplitude H_{drive} defines the "field of view". It is as big as needed to move the field free point x_{FFP} (defined by $H(x_{FFP}(t),t) = 0$) at least from $x_{min} = -L/2$ to $x_{max} = L/2$, to scan the whole phantom. The time interval considered within the simulation starts at $t = 0$ and ends at $t = T_{drive}$, with $T_{drive} = 1/\omega_{drive}$. Time discretization (as described in 4.1.1) yields the timestamps t_i.

With the magnetic field and time definitions above, the FFP trajectory $x_{FFP}(t)$ is a "1D Lissajous trajectory", crossing each point of the phantom two times.

Real signal generation

The signal from the phantom is simulated via MMF2, using the properties of the phantom and $H(x,t)$ as input. Actually, for each pixel i with location x_i the relative magnetization[1] for all times $M_i(t_i)$ is calculated separately. Then, all $M_i(t_i)$ are summed up (weighted equally) and the result is normalized, yielding the time-dependent relative magnetization response $M(t_i)$ of the entire phantom.

For image reconstruction in terms of the DFM, the *non-linear part* of the *detected* signal is required, i.e. the inductively detected magnetization response without the linear response part. Therefore, the

[1] Since all rectangles in the phantom are of same height (concentration), it is sufficient to consider the *relative* magnetization.

fundamental frequency component ω_{drive} is removed from the FOURIER spectrum of $\frac{d}{dt}M(t_i)$. The result is transformed back into the time domain (via inverse FOURIER transformation), yielding the signal vector $\vec{A}$ as described in Equation 2.46. The course of the signal over the time is presented in the central graph of Figure 4.11.

During image reconstruction, $\vec{A}$ will be decoded using a reconstruction kernel $\mathbf{S}$ to gain the concentration distribution $c_{reco}(x)$.

Reconstruction kernel generation

As explained in part 2.6.3 ("Drive Field Method: DFM reconstruction scheme"), the reconstruction kernel $\mathbf{S}$ (a matrix, cf. Equation 2.46), has to be obtained by acquisition of the signals $\vec{A}_{ds,i}$ of many single delta samples with *known* concentration $c_0(\rho_0)$.

The signals $\vec{A}_{ds,i}$ are gained via relative magnetization simulations using the SPM. Since the SPM is concentration-independent, c_0 is set indirectly by using an effective diameter, which is found as described in 4.2.2 ("Impact of particle concentration: effective particle diameter"). Three reconstruction kernels $\mathbf{S}$ were built, using three different diameters:

- The optimal one:
  representing $c_{Fe_3O_4} = 1\,\text{mol/l} \rightarrow d_{eff} = 17.3\,\text{nm}$.
- An overestimated one:
  representing $c_{Fe_3O_4} = 1.6\,\text{mol/l} \rightarrow d_o = 21.1\,\text{nm}$.
- An underestimated one:
  representing $c_{Fe_3O_4} = 0.3\,\text{mol/l} \rightarrow d_u = 15.6\,\text{nm}$.

Reconstruction result

The reconstruction was accomplished according to Equation 2.46. The result is presented in the bottom graph of Figure 4.11.

Since the reconstruction is based on solving a linear system of equations, it assumes a *linear* relation between amplitudes and concentration. As argued in 3.2, reality does not satisfy this. In case of $\mathbf{S}$ gained via SPM using d_{eff}, the "calibration point" of the linear reconstruction

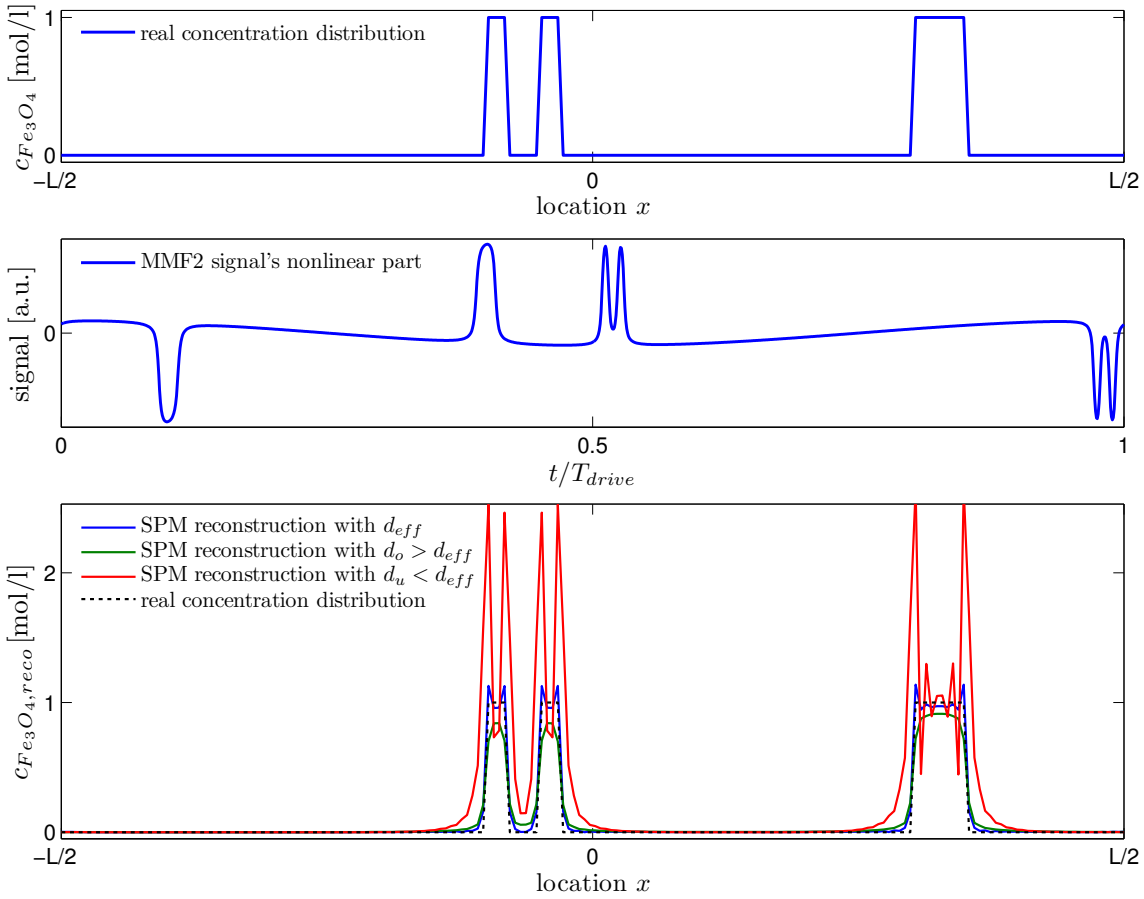

Figure 4.11: 1D MPI simulation using the drive field method (DFM). Top: 1D concentration distribution (phantom). Center: Nonlinear signal part due to the excitation given by Equation 4.12; simulated via MMF2. Bottom: Reconstruction using three different kernels, obtained via SPM with three different particle sizes. d_{eff} corresponds to $c_{Fe_3O_4} = 1$ mol/l, the concentration in a few places of the phantom.

matches the non-linear reality for $c_{Fe_3O_4} = 1$ mol/l. Hence, the reconstruction kernel created with d_{eff} yields the best "image" $c_{Fe_3O_4,reco}(x)$. The other reconstruction kernels are expected to provide worse results.

This simulation shows that the linear reconstruction method used is unsuitable for quantitative image reconstructions in MPI. Only the concentration c_0 used for calibration is decoded properly. If the phantom exhibits other concentration values, their quantitative reconstruction fails. Furthermore, the spatial resolution decreases, depending on the difference between concentrations found in the phantom and c_0. This behavior can be observed best by means of the d_u-reconstruction (red line).

Due to the non-linear dependence of higher harmonic amplitudes on particle concentration, linear reconstruction methods should be inappropriate for quantitative reconstruction in general. Further effort has to be expended on developing non-linear schemes or at least on minimizing the errors made due to linear reconstructions.

Chapter 5

Signal characterization by experiment

5.1 MPS concentration dependency

As a result of the discussion in 3.2 and the simulations described in 4.2.2, a non-linear relation between the amplitude A_n of a single harmonic n and the ferrofluid concentration c is expected to occur in a real MPS experiment, too. An experimental MPS setup was used to

- prove the deviation of the SPM from the reality, manifesting itself in a *non-linear* relation between the two quantities A_n and c.
- check the suitability of MMF2 to predict $A_n(c)$.

5.1.1 Experimental MPS setup

A *general* scheme of a "magnetic particle spectrometer" is shown in Figure 5.1. This part describes the actual realization of the apparatus used in the experiments.

The *harmonic drive circuit* is based on a signal generator, two integrated audio-amplifier chips in parallel (LM3886T, National Semiconductor) and a solenoid as *transmission coil* (field homogeneity in the volume of the ferrofluid sample $\geq 99\,\%$; 340 windings; length $7\,\mathrm{cm}$;

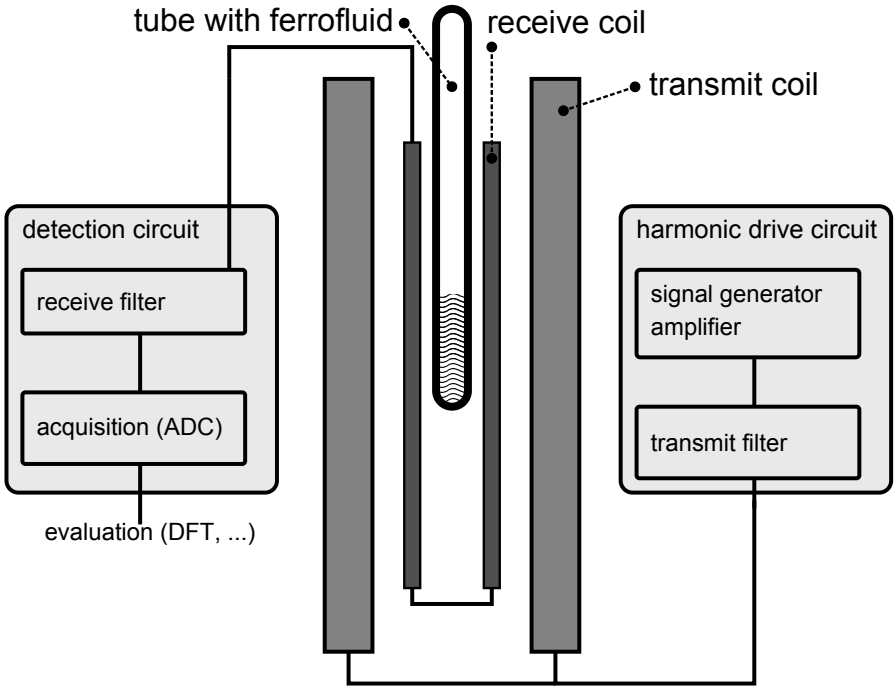

Figure 5.1: General experimental scheme of a "magnetic particle spectrometer". The goal of the *harmonic drive circuit* is to drive the *transmit coil* with a strong and harmonically oscillating current. Coils and ferrofluid sample are shown as cross-section. In the *detection circuit*, the *receive filter* masks out the fundamental frequency of the excitation to only detect the non-linear response. Signal acquisition is done with an ADC (analog-digital-converter).

inner diameter $3\,\mathrm{cm}$; central field efficiency $6\,\mathrm{mT/A}$). During all experiments, the current in the transmit coil was held constant ($0.95\,\mathrm{A}$ RMS at $15.65\,\mathrm{kHz}$). A *transmit filter* as indicated in Figure 5.1 was not used. In a more sophisticated setup, its purpose is to absolutely minimize any other frequency components than the desired fundamental frequency of the transmit signal.

During measurement, the ferrofluid sample is centered within the receive coil, which itself is centered within the transmit coil.

The *receive coil* is made of litz wire (field homogeneity $\geq 96\,\%$; 800 windings; length $4\,\mathrm{cm}$; inner diameter $5.5\,\mathrm{mm}$). In the *detection circuit* (cf. Figure 5.1), the *receive filter* is an 11-pole Type I CHEBYSHEV high-pass filter [43], effectively damping detected harmonics up to

the cutoff frequency at 99.4 kHz. Filter characteristic and excitation frequency optimize the setup for detecting the 7th harmonic ($n = 7$). Low-noise amplified (AD604, Analog Devices) time signal *acquisition* is done with a digital storage oscilloscope (TDS1001, Tektronix). To obtain a high signal to noise ratio, all recorded time signals are averaged 128 times before evaluation (DFT) in MATLAB. Here, systematic errors are minimized by evaluating the difference between the signal with and without a sample within the receive coil.

Series of measurements with different ferrofluid samples

The higher harmonic amplitudes A_n were analyzed for one ferrofluid at five different iron concentrations $c_{Fe,i}$. The volume of the ferrofluid was the *same* for each sample. Therefore, the difference in total amount of substance between two samples is proportional to the concentration difference.

We used a customized ferrofluid (as described in [44]), consisting of dextran coated magnetite cores with water as solvent. The ferrofluid can be considered as *monodisperse*, with $d = 8.5$ nm. The iron concentrations $c_{Fe,i}$ [mol/l] are from production and measurement (ultraviolet-visible spectrophotometry). The values are listed in column 1 of Table 5.1. The error in $c_{Fe,i}$, which is estimated generously to ± 0.02 mol/l, is considered to be the dominating error in the experiments[1].

5.1.2 Result

The experimental result for the 7th and 9th harmonic of the MPS signal is presented in Table 5.1. Further harmonics could not be detected well for the lowest concentrations $c_{Fe,i}$. $A_{7,exp}(c_{Fe,i})$ is visualized in Figure 5.2. Furthermore, the graph contains the linear relation given by the first two data points, since the SPM is only correct in the limit $c_{Fe} \to 0$. Systematic deviations of the data points from the linearity imply that the measured signal amplitudes are *non-linear* dependent on $c_{Fe,i}$. The non-linear $A_n(c_{Fe,i})$ dependency was also verified for $A_{9,exp}(c_{Fe,i})$.

[1] While the real error in $c_{Fe,i}$ is smaller, this generous estimation outweighs the small error in A and the error in the volume of the ferrofluids. A more detailed error discussion is omitted, since it is used only during graphical interpretation.

$c_{Fe,i}$ [$\frac{\text{mol}}{\text{l}}$]	$A_{7,exp}$ [a.u.]	$A_{9,exp}$ [a.u.]	$\frac{A_{7,exp}}{A_{9,exp}}$
0.02 ± 0.02	0.12086	0.00036	334.1
0.12 ± 0.02	0.71715	0.00229	313.8
0.20 ± 0.02	1.25552	0.00403	311.2
0.63 ± 0.02	4.32175	0.01454	297.2
1.17 ± 0.02	10.31910	0.03621	285.0

Table 5.1: Experimentally obtained higher harmonic amplitudes $A_{7,exp}$ and $A_{9,exp}$ in the MPS signal of a ferrofluid at five different iron concentrations $c_{Fe,i}$. For the experimental setup, confer 5.1.1.

It is important to stress that the *ratio* of the 7th and 9th harmonic significantly changes with increasing concentration (cf. column 4 of Table 5.1). The harmonic with higher n gains weight. This is an **unambiguous and quantitative evidence** for increasing interparticle interactions, as explained in 4.2.2 ("Impact of particle concentration: Impact of local particle concentration on MPS").

5.2 Comparison with simulation

To check the suitability of MMF2 for predicting $A_n(c)$ quantitatively, an MPS simulation was accomplished, using all parameters as given by the experiment. Thus, M_s is set to 480000 A/m (magnetite) and d is set to 8.5 nm. The excitation field amplitude used is 6 mT/A$\cdot 0.95$ A$\cdot\sqrt{2} \approx 8$ mT. Since the total amount of magnetic substance within the measured ferrofluid samples changes linearly with increasing $c_{Fe,i}$, the *total* MMF2 magnetization was simulated, exhibiting this characteristic, too. In parallel, the total magnetization as given by the SPM was simulated with the same parameters. If the MMF2 simulation properly reflects reality, the measured data points $A_{n,exp}(c_{Fe,i})$ must be reproducible by multiplying the whole simulated curve $A_{n,MMF2}(c_{Fe})$ with one constant factor K[1].

[1] Many properties of the experiment have *linear* impact on the measured numbers $A_{n,exp}(c_{Fe,i})$: the volume of the ferrofluid sample, the receive coil sensitivity, receive filter characteristics, low-noise amplification, etc. These numbers are not

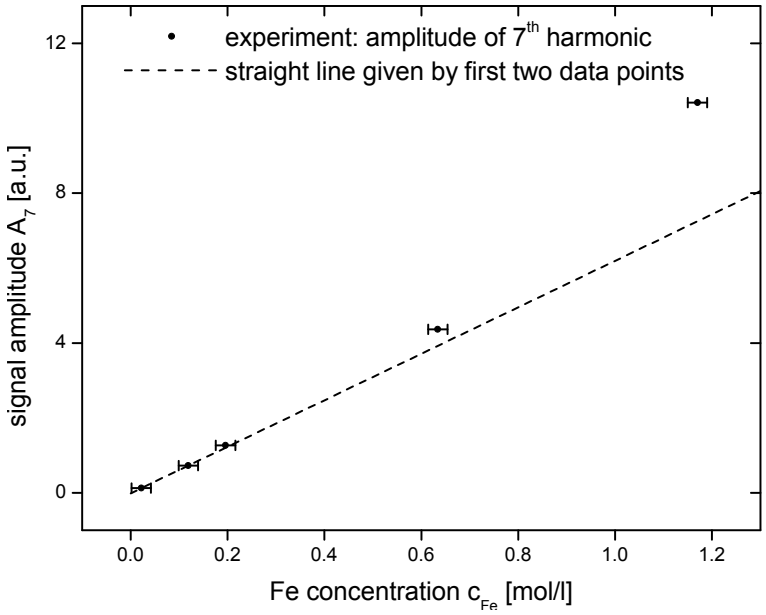

Figure 5.2: Measured 7th harmonic amplitude A_7 in arbitrary units (a.u.) of the MPS signal in dependence on iron concentration $c_{Fe,i}$. The straight line is the linearity given by the first two data points.

By doing so[1], the MMF2 curves very well reproduce both amplitudes $A_{7,exp}(c_{Fe,i})$ and $A_{9,exp}(c_{Fe,i})$, as can be seen in Figure 5.3. Hence, MMF2 describes the magnetization response of real ferrofluids very well and – in particular – allows to predict the generation of higher harmonics in a real MPI/MPS setup.

The SPM simulation was multiplied with the same factor K and the resulting curves (straight lines, due to their paramagnetic nature) are shown in the graphs, too. Thus, the difference between the SPM and MMF2 curves again visualizes the inadequacy of the SPM in case of

known exactly, but can be unified to one single constant of proportionality. The factor K exploits this degree of freedom and can be used to adjust the results of the simulation to the experimental ones.

[1] K was found separately for each harmonic. This was done, because the receive circuit of the experimental setup contains only approximately known frequency dependencies. With exact quantitative knowledge about of these non-linear impacts, it is possible to compare experimentally gained amplitude *ratios* with theoretically predicted ratios, and therefore to validate MMF2 on a higher level.

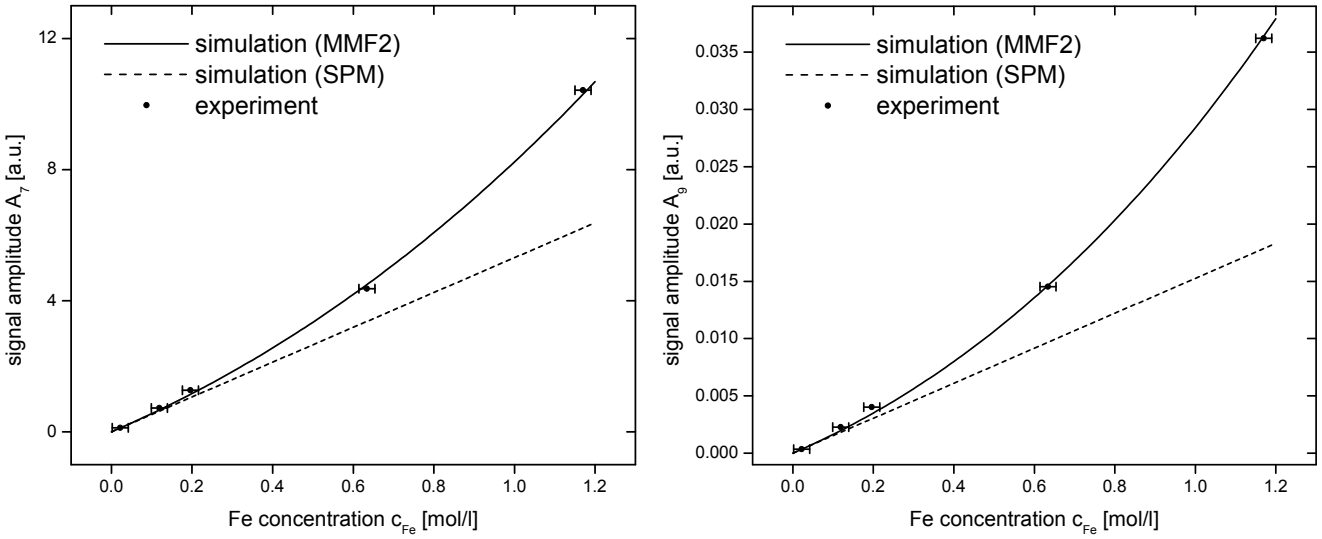

Figure 5.3: Experimentally gained amplitudes of the 7^{th} (left) and 9^{th} (right) harmonic of the MPS signal of five ferrofluid samples, exhibiting different iron concentration c_{Fe}; in comparison with MMF2 and SPM simulations.

dense ferrofluids.

As already mentioned in 4.2.2, local particle densities significantly exceeding the scope of validity of the SPM will not be uncommon in real MPI applications. Hence, it is necessary to always bear particle coupling effects in mind. While there will be many MPI applications exhibiting very low particle concentrations, there will be specific cases with drastic impact of concentration effects, considering e.g. the agglomeration of magnetic particles in cells (leading to iron concentrations of $0.2 - 5$ mol/l [42]).

Chapter 6

Application: molecular detection of a substance/process

Working on the theoretical understanding of the generation of the MPS signal and the experimental verification of the significance of the concentration effect, lead to an idea for an application:

> ***"Evidence of a substance or process on the cellular and molecular level by means of detecting variations in the non-linear magnetization response of magnetic markers."***

In the framework of the proposed method, those substances/processes are confirmable, whose existence/run leads to a biological or chemical reaction changing the physical properties of specific magnetic markers in such a way that their non-linear magnetization response varies in a detectable manner.

6.1 Classification

The purpose of the invention is to prove the existence of a specific substance or process in a quick, cheap and uncomplicated way, based

on magnetic particle spectroscopy. Potentially detectable substances are e.g. cells, viruses, bacteria, proteins or smaller molecules. Examples for detectable processes are the decomposition of magnetic particles (e.g. driven by metabolism) or the cell internalization of particles.

The most important effect exploited by the invention is the non-linear dependency of higher harmonic amplitudes in the MPS signal on *local* particle concentration changes (cf. theory: 3.2, simulation: 4.2.2, experiment: 5.1). Another exploitable effect is the signal change due to magnetic core diameter and total amount of magnetic substance variations in the investigated volume.

The success of the method and its fields of application entirely depend on the availability of *specifically* adjusted magnetic markers, which have to be used to exploit the effects named above for evidence of a specific substance/process. Consider e.g. a coating of magnetic markers, adjusted to connect to the surface of a specific substance or adjusted to enter specific cells. **Contact between the markers and the substance or cells, then leads to an increased local particle concentration**.

The invented method is based on measuring *changes*. Therefore, at least two measurements are needed to draw conclusions. Furthermore, it is easily conceivable to accomplish many measurements with high repetition rate to observe processes in real-time.

6.1.1 The (commercial) relevance of the method

The company T2BIOSYSTEMS [45] already realized a method to verify the existence of a substance in a commercially available apparatus. On a molecular level, the idea is identical: they make use of local concentration changes of magnetic particles, due to the existence of the target substance. However, the detection of concentration changes is done via *nuclear magnetic resonance* (NMR): the $T2$ relaxation constant of water, which is surrounding the magnetic particles, depends on the concentration of the particles. The general method is explained in e.g. [46]. There, the authors demonstrated that their technique can be readily applied for detecting tuberculosis, by proving the existence of the *Mycobacterium tuberculosis*.

The method proposed here, replaces NMR by MPS to detect changing magnetic properties of the magnetic particles. As a consequence,

existing knowledge regarding the "nano-engineering"[1] can be adopted unaltered. The important point is that the MPS-based method promises to be less expensive and better (faster, more sensitive) than the NMR-based method, as will be discussed in 6.2.2.

6.2 Details

6.2.1 Local particle agglomeration due to special particle shells

Consider a ferrofluid, made of magnetic particles with specific shells, adjusted to a target substance, as shown in Figure 6.1 A. Due to its chemical properties, the shell should bind to the surface of a single unit of the target substance (e.g. to a single cell or virus), see Figure 6.1 C. Another possibility is that a single unit of the target substance is smaller than the magnetic particles (this could be a protein or a smaller molecule) and provides tight binding between them, as shown in 6.1 B.

If the target substance is mixed with the considered special ferrofluid, the magnetic particles tightly bind to surfaces (Figure 6.1 E) or tightly stick together due to a linking effect (Figure 6.1 D). This **particle agglomeration** or **particle cluster formation** leads to an increased local particle concentration, yielding a significant change of higher harmonic amplitudes and – in particular – amplitude ratios, in comparison with a reference measurement (cf. part 4.2.2: "Impact of local particle concentration on MPS").

Specific particle shells may also lead to a preferred absorption by special cells, resulting in very high particle concentrations within the cells.

6.2.2 Comparison with the NMR method

Hardware

Excitation frequencies in MPS are below 100 kHz. Therefore, audio components can be used in the excitation circuit. The detection circuit

[1] Adjustment of magnetic particles and/or particle shells to specific substances/processes.

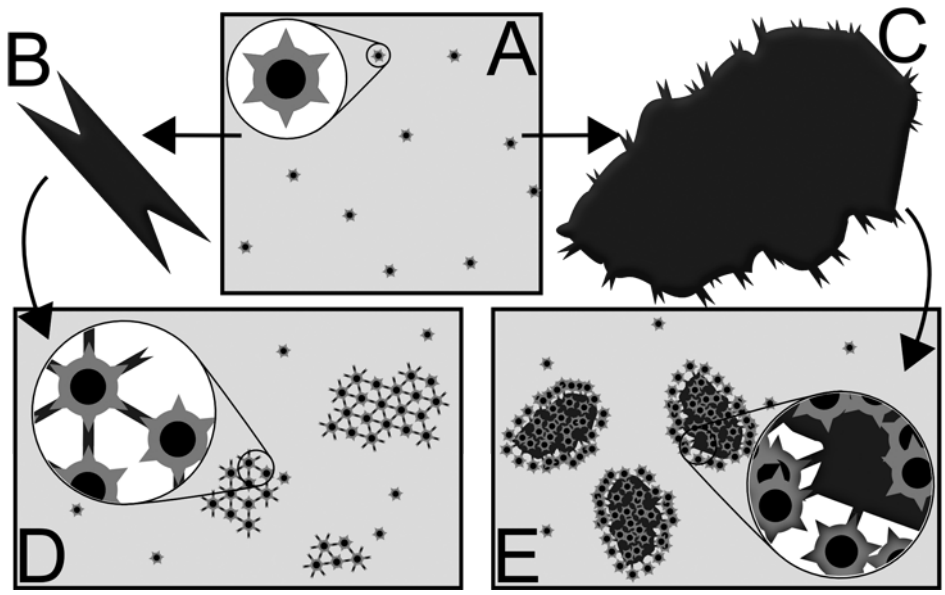

Figure 6.1: **A**: a ferrofluid made of special magnetic markers (magnetic cores (black) in special shells (dark-gray)). **B**: a substance to be tested for; a single element is smaller than one marker particle; one element is able to connect the particles tightly. **C**: another substance to be detected; bigger than the particles; is able to tightly bind many particles tightly on its surface. **D and E**: ferrofluids with agglomerated magnetic markers due to the existence of substances to be tested for.

should be able to detect several higher harmonics. For an excitation frequency from 10 to $100\,\mathrm{kHz}$, an upper detection limit of $1\,\mathrm{MHz}$ already covers the 9^{th} or even higher harmonics.

For NMR measurements, a strong static magnetic field is required besides excitation and detection circuits. Depending on its actual field strength, the nuclear spin resonance frequency is on the order of 10 to $100\,\mathrm{MHz}$. Excitation of the system is done by irradiating this resonance frequency as precisely as possible; detection is performed at the same frequency. These high frequencies, the strong offset field and the required precision of the excitation renders NMR hardware more expensive and less robust than MPS hardware.

Repetition rate of single experiments

The duration of a single MPS experiment is on the order of $10\,\mu s$, considering a reasonable excitation frequency and only a few periods to analyze spectroscopically. In case of NMR, between two measurements the magnetic relaxation process (which lasts on the order of $100\,ms$ up to seconds) has to be waited for.

Hence, MPS allows for a much higher repetition rate of single experiments. This can be exploited for averaging a lot or for real-time measurements.

Signal background

The NMR method analyzes signal emitted by water. Even if *all* magnetic particles in the analyzed volume agglomerate, this changes the signal of a only a part of the emitting system. Unaffected water creates a disturbing background signal.

The MPS method analyzes the signal emitted by magnetic particles. If all magnetic particles agglomerate, the whole signal-producing system changes. There is no such background as described for the NMR method.

Sensitivity

The sensitivity of single experiments of either the MPS or NMR method is difficult to compare. The comparison can be based on the estimation that a magnetic particle in MPS provides the same magnetization as 10^{14} protons in NMR[1].

In principle, the lack of background signal in case of the MPS method should be a huge advantage. In combination with the higher single experiment repetition rate, the MPS method should exhibit a higher sensitivity per time than the NMR method.

[1] Considering the magnetic moment of a proton being $10^{-26}\,Am^2$, the magnetic moment of a magnetic particle being $10^{-18}\,Am^2$ and 1 contributing spin of 1000000 in NMR.

6.2.3 Extensions

Optimization via offset field

As described in part 2.5.2, the generation of higher harmonics can be optimized by application of a magnetic offset field H_{off}. The spectroscopical investigation of a ferrofluid sample is then done by applying the field

$$H(t) = H_{off} + H_{exc}\sin(\omega_0 t) \tag{6.1}$$

to the total volume of the sample. For substance verification based on concentration changes, H_{off} can be chosen in a way that a concentration change leads to a maximum change of higher harmonic amplitudes.

Spatially resolved evidence: combination with MPI

In principle, the proposed method for evidence of a substance or process can be combined with the MPI approach, using the same specifically developed magnetic markers as described before. Comparison of two MPI measurements should *spatially resolved* reveal the changes of amplitudes of higher harmonics exhibiting the fingerprint of strong concentration changes. It is – at least theoretically – possible to find these fingerprints; the capability has to be created by developing special reconstruction schemes.

Chapter 7

Conclusion

In previous works in the field of Magnetic Particle Imaging (MPI), magnetic particle interaction was disregarded by only considering LANGEVIN's single particle model (SPM). Within this thesis, the impact of interacting particles on the MPI signal was treated theoretically, by simulation, and by experiment.

The most important result of this work is that magnetic particle interaction leads to a non-linear relation between higher harmonic amplitudes A_n and particle concentration c. Therefore, current linear image reconstruction schemes are not qualified for quantitative reconstruction of the spatial particle concentration distribution: only the reference particle concentration used for detecting the system function is reconstructed properly; other concentrations found in a phantom are decoded wrongly. Furthermore, the spatial resolution suffers.

It was shown that the impact of increasing local particle concentration qualitatively is the same as the impact of a magnetic core diameter enhancement. Hence, ferrofluids based on cluster particles (several magnetic cores per particle) can be described by an effective magnetic core diameter per particle. Comparison of simulation and experiment revealed that the second-order modified mean-field theory (MMF2) by IVANOV is suitable for predicting the magnetization response of a dense ferrofluid. Therefore, MMF2 is the preferable theory in MPI, predicting the non-linear $A_n(c)$ relation correctly.

The main conclusion of this thesis is that magnetic particle interaction is an important part in the theory of MPI. In the future, it

has to be accounted for in image reconstruction schemes, to maintain the capability of quantitative analysis even in cases of strong local concentration fluctuations, e.g. when particles agglomerate in cells.

Moreover, **the effect of magnetic particle interaction on the MPI signal opens up a new field of application**, by observing the characteristic fingerprint of local particle concentration changes: the change of the ratio of two higher harmonic amplitudes. This can be used to follow the process of particle agglomeration in cells or to prove the existence of a specific substance on the cellular and molecular level, like bacteria, viruses, cells, proteins or smaller molecules.

Bibliography

[1] B. Gleich and J. Weizenecker. “Tomographic imaging using the nonlinear response of magnetic particles”. In: *Nature* 435 (2005), pp. 1214–1217. See pp. 1, 30, 33, 35, 64.

[2] J. Weizenecker et al. “Three-dimensional real-time in vivo magnetic particle imaging”. In: *Phys. Med. Biol.* 54 (2009), pp. L1–L10. See pp. 1, 2, 35.

[3] P. Hofmann. *Solid State Physics*. Wiley VCH Verlag GmbH, 2008. See pp. 4, 10.

[4] A. Aharoni. *Introduction to the Theory of Ferromagnetism*. Oxford University Press, 2001. See pp. 5, 6, 10.

[5] KJ. Klabunde, ed. *Nanoscale Materials in Chemistry*. John Wiley & Sons, 2001. See pp. 6, 8, 9.

[6] AI. Gusev and AA. Rempel. *Nanocrystalline Materials*. Cambridge Intl Science Pu, 2003. See p. 6.

[7] E. Du Tremolet de Lacheisserie, D. Gignoux, and M. Schlenker. *Magnetism Fundamentals*. Springer, 2005. See p. 7.

[8] L. Marton, ed. *Advances in Electronics and Electron Physics*. Academic Press Inc, 1979. See pp. 8, 9.

[9] RE. Rosensweig. *Ferrohydrodynamics*. Cambridge University Press, 1985. See p. 11.

[10] MH. Sousa. “NiFe2O4 nanoparticles in ferrofluids: evidence of spin disorder in the surface layer”. In: *JMMM* 242-245, part 1 (2002), pp. 572–574. See p. 12.

[11] M. Hayat, ed. *Cancer Imaging: Instrumentation and Applications Volume 2*. Elsevier LTD, Oxford (Academic Press), 2007. See pp. 12, 13.

[12] L. Matuszewski et al. “Molekulare und parametrische Bildgebung mit Eisenoxiden”. In: *Der Radiologe* 47 (2007), pp. 34–42. See p. 13.

[13] Y. Jun, JH. Lee, and J. Cheon. “Chemisches Design von leistungsfähigen Nanosonden für die Kernspintomographie”. In: *Angew. Chem.* 120 (2008), pp. 5200–5213. See p. 13.

[14] Y. Bao and KM. Krishnan. “Preparation of functionalized and gold-coated cobalt nanocrystals for biomedical applications”. In: *JMMM* 293 (1) (2005), pp. 15–19. See p. 13.

[15] PC Moraisa et al. “Preparation and characterization of ultrastable biocompatible magnetic fluids using citrate-coated cobalt ferrite nanoparticles”. In: *Thin Solid Films* 515 (1) (2006), pp. 266–270. See p. 13.

[16] J. Rahmer et al. “Signal encoding in magnetic particle imaging: properties of the system function”. In: *BMC Medical Imaging* 9 (2009), p. 4. See p. 14.

[17] Ritter von Burg. *Compendium der höheren Mathematik*. 1859, p. 218. See p. 20.

[18] Martin Rückert. “Untersuchung und Beschreibung der Signalentstehung im Magnetic Particle Imaging”. Diploma thesis. Universität Würzburg, 2008. See pp. 24, 68.

[19] M. Cerdonio et al. “Variability of the magnetic moment of carbon monoxide hemoglobin from carp”. In: *Proc. Nati. Acad. Sci. USA* 77 (1980), pp. 1462–1465. See p. 29.

[20] SM. Dubiel et al. “Magnetic properties of human liver and brain ferritin”. In: *Eur Biophys J* 28 (1999), pp. 263–267. See p. 29.

[21] J. Weizenecker, B. Gleich, and J. Borgert. “Magnetic particle imaging using a field free line”. In: *J. Phys. D: Appl. Phys.* 41 (2008), p. 105009. See p. 30.

[22] R. Lefever. “4.1.1.1 Summary of physical and magnetic properties”. In: *Landolt-Börnstein - Group III Condensed Matter* 12b: Part B: Spinels, Fe Oxides, and Fe-Me-O Compounds (1980). See pp. 31, 40.

[23] RW. Chantrell, J. Popplewell, and SW. Charles. “Measurements of particle size distribution parameters in ferrofluids”. In: *IEEE T. Magn.* 14 (1978), p. 975. See pp. 41, 48.

[24] S. Biederer et al. “Magnetization Response Spectroscopy of Superparamagnetic Nanoparticles for Magnetic Particle Imaging”. In: *Journal of Physics D: Applied Physics* 42.20 (2009), 7pp. See pp. 41, 65.

[25] RM. Ferguson, KR. Minard, and KM. Krishnan. “Optimization of nanoparticle core size for magnetic particle imaging”. In: *JMMM* 321 (2009), pp. 1548–1551. See p. 41.

[26] KI. Morozov and AV. Lebedev. “The effect of magneto-dipole interactions on the magnetization curves of ferrocolloids”. In: *JMMM* 85.1-3 (1990), pp. 51–53. ISSN: 0304-8853. See pp. 41, 47.

[27] AF. Pshenichnikov, VV. Mekhonoshin, and AV. Lebedev. “Magneto-granulometric analysis of concentrated ferrocolloids”. In: *JMMM* 161 (1996), pp. 94 –102. ISSN: 0304-8853. See pp. 43, 44, 47, 48.

[28] DE. Koppel. “Analysis of Macromolecular Polydispersity in Intensity Correlation Spectroscopy: The Method of Cumulants”. In: *J. Chem. Phys.* 57.11 (1972), pp. 4814–4820. See p. 44.

[29] AF. Pshenichnikov. “Equilibrium magnetization of concentrated ferrocolloids”. In: *JMMM* 145 (1995), pp. 319–326. See pp. 46, 47.

[30] MI. Shliomis et al. “Magnetic properties of ferrocolloids”. In: *JMMM* 85 (1-3) (1990), pp. 40–46. See p. 47.

[31] KI Morozov et al. “Magnetic properties of ferrocolloids: the effect of interparticle interactions”. In: *JMMM* 65 (1987), pp. 269–272. See p. 47.

[32] AO. Ivanov and OB. Kuznetsova. “Magnetic properties of dense ferrofluids: An influence of interparticle correlations”. In: *Phys. Rev. E* 64 (2001), p. 041405. See pp. 47, 49.

[33] AO. Ivanov et al. “Magnetic properties of polydisperse ferrofluids: A critical comparison between experiment, theory, and computer simulation”. In: *Phys. Rev. E* 75 (2007), p. 061405. See pp. 47–49.

[34] R. Kaiser and G. Miskolczy. “Magnetic Properties of Stable Dispersions of Subdomain Magnetite Particles”. In: *J. Appl. Phys.* 41 (1970), pp. 1064–1072. See p. 48.

[35] *Fourier Analysis in MATLAB*. URL: http://www.mathworks.com/moler/fourier.pdf. See p. 52.

[36] *Computing Fourier Series and Power Spectrum with MATLAB*. URL: http://faculty.olin.edu/bstorey/Notes/Fourier.pdf. See p. 52.

[37] Albert H. Kaiser. *Digital Signal Processing using the Fast Fourier Transform (FFT)*. 1997. See p. 53.

[38] *Fastest Fourier Transform in the West*. URL: http://fftw.org. See p. 55.

[39] *IEEE Std 754-2008: Standard for Floating-Point Arithmetic*. 2008. See p. 58.

[40] *Magnetit*. URL: http://de.wikipedia.org/wiki/Magnetit. See p. 61.

[41] R. Lawaczeck et al. “Magnetic iron oxide particles coated with carboxydextran for parenteral administration and liver contrasting. Pre-clinical profile of SH U555A.” In: *Acta Radiol.* 38 (1997), pp. 584–97. See p. 65.

[42] C. Billotey et al. “Cell Internalization of Anionic Maghemite Nanoparticles: Quantitative Effect on Magnetic Resonance Imaging”. In: *Magn Reson Med* 49(4) (2003), pp. 646–654. See pp. 66, 80.

[43] Steve Winder. *Analog and Digital Filter Design*. 2002. See p. 76.

[44] R Beringer. “Synthese von Eisenoxid-Nanopartikeln als MR-Kontrastmittel”. Diploma thesis. Julius-Maximilian-Universität Würzburg, 2007. See p. 77.

[45] *T2Biosystems*. URL: http://www.t2biosystems.com. See p. 82.

[46] H. Lee, TJ. Yoon, and R. Weissleder. “Ultrasensitive detection of bacteria using core-shell nanoparticles and an NMR-filter system”. In: *Angew Chem* 48(31) (2009), pp. 5657–5660. See p. 82.

Appendices

Appendix A: Mathematica source codes

A.1) Magnetic Particle Spectroscopy: schematical simulation

Excitation:	**harmonical & symmetrical with respect to the origin**
Transfer function:	**Langevin function $\mathcal{L}(\alpha)$ as a representation for any specific magnetization theory M(H)**
Response:	**inductive detection (time derivative)**

Signal generation: *M(t)* and $\frac{d}{dt}M(t)$

In[1]:=
```
Langevin[α_] = Coth[α] - 1 / α;
MagnField[t_] = 6 * Sin[t];
MagnResponse[t_] = Langevin[MagnField[t]];
DdtMagnResponse[t_] = D[MagnResponse[t], {t, 1}]
```

Out[4]=
$$\frac{1}{6}\,\text{Cot}[t]\,\text{Csc}[t] - 6\,\text{Cos}[t]\,\text{Csch}[6\,\text{Sin}[t]]^2$$

Careful setup of sampling parameters for DFT

```
fdrive = 1 / (2 * Pi);
fsample = 50 * fdrive;
periods = 1;
length = periods / fdrive;
deltat = 1 / fsample; (* distance of sampling points *)
(* crucial: [sampled dataset]+[sampled dataset]+... MUST BE the periodic signal
     --> first and last sampled point MUST NOT be the same.
     --> Therefore, sample points in time from zero in distances deltat
         up to length-deltat *)
tvec = Table[time, {time, 0, length - deltat, deltat}];
samplepoints = Length[tvec];
deltaf = fsample / samplepoints;
```

Build frequency vectors: absolute and normalized

In[13]:=
```
freqvec = Table[freq, {freq, 0, fsample - deltaf, deltaf}];
freqvecnorm = freqvec / fdrive;
```

Sample signals and correct $\mathcal{L}(0)=0$

In[21]:=
```
MagnResponseSamples = Map[MagnResponse, tvec];
MagnResponseSamples[[1]] = 0;
MagnResponseSamples[[26]] = 0;
DdtMagnResponseSamples = Map[DdtMagnResponse, tvec];
DdtMagnResponseSamples[[1]] = 2;
DdtMagnResponseSamples[[26]] = -2;
```

Build correctly normalized DFTs with 200 digit precision

- **Frequency spectrum of magnetization response *M(t)***

In[27]:=
```
RespSpectrum = 2 * Abs[Fourier[
       N[MagnResponseSamples, 200], FourierParameters → {1, -1}
      ]] / samplepoints;
RespSpectrum[[1]] = RespSpectrum[[1]] / 2;
```

- **Frequency spectrum of $\frac{d}{dt}M(t)$**

In[29]:=
```
DdtRespSpectrum = 2 * Abs[Fourier[
       N[DdtMagnResponseSamples, 200], FourierParameters → {1, -1}
      ]] / samplepoints;
DdtRespSpectrum[[1]] = DdtRespSpectrum[[1]] / 2;
```

- **Frequency spectrum of $\frac{d}{dt}M(t)$ via $i\omega$ multiplication**

In[31]:=
```
DdtFreqMultiRespSpectrum = 2 * Abs[i * 2 * π * freqvec * Fourier[
        N[MagnResponseSamples, 200], FourierParameters → {1, -1}
       ]] / samplepoints;
DdtFreqMultiRespSpectrum[[1]] = DdtFreqMultiRespSpectrum[[1]] / 2;
```

Build Amplitude-Frequency-Pair lists for plotting, cut out numerical zeros

In[33]:=
```
ZeroPositions = Position[Chop[RespSpectrum], 0];
RespSpectrumZeroClean = Delete[RespSpectrum, ZeroPositions];
freqvecnormZeroClean = Delete[freqvecnorm, ZeroPositions];
DdtZeroPositions = Position[Chop[DdtRespSpectrum], 0];
DdtRespSpectrumZeroClean = Delete[DdtRespSpectrum, DdtZeroPositions];
DdtFreqMultiZeroPositions = Position[Chop[DdtFreqMultiRespSpectrum], 0];
DdtFreqMultiRespSpectrumZeroClean = Delete[
   DdtFreqMultiRespSpectrum,
   DdtFreqMultiZeroPositions];
maxpoints = Round[Length[DdtRespSpectrumZeroClean ] / 3];
DdtplotdataLog = Table[
   {freqvecnormZeroClean[[i]], DdtRespSpectrumZeroClean[[i]]},
   {i, 1, maxpoints}];
DdtFreqMultiplotdataLog = Table[
   {freqvecnormZeroClean[[i]], DdtFreqMultiRespSpectrumZeroClean[[i]]},
   {i, 1, maxpoints}];
plotdata = Table[
   {freqvecnormZeroClean[[i]], RespSpectrumZeroClean[[i]]},
   {i, 1, maxpoints}];
```

- **Plotting example: Frequency spectrum of $\frac{d}{dt}M(t)$ via both methods**

In[44]:=
```
ListPlot[{DdtplotdataLog, DdtFreqMultiplotdataLog},
 Axes → False, Filling → Bottom, Frame → True,
 FrameLabel → {{Style["∝ ℱ(U(t))", 21], None}, {Style["ω/ω₀", 21], None}} ,
 LabelStyle → Directive[Bold, 12, FontFamily → "Times"],
 PlotStyle → {Directive[PointSize[0.025], Gray], Directive[PointSize[0.009], Black]},
 FillingStyle → {Directive[Thickness[0.005], Black]},
 ImageSize → 400
]
```

Out[44]=

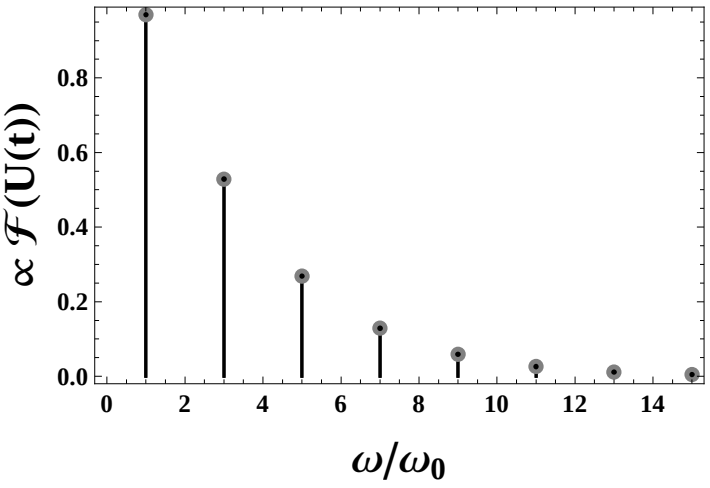

A.2) Magnetic Particle Spectroscopy: Harmonic's exponential decay in dependence of magnetic core diameter

Excitation:	**harmonical & symmetrical with respect to the origin**
Transfer function:	**relative magnetization as given by SPM, for different diameters**
Response:	**inductive detection (time derivative)**
Evaluation:	**exponential fit of odd harmonics' amplitudes**

Physical parameters and magnetization theory

In[410]:=
```
μ0 = 4 * Pi * 10^(-7);
kB = 1.3806504`500 * 10^(-23);
T = 300;
ampdrive = 5 / 1000;
M0 = 480 000;
Bdrive[time_] = ampdrive * N[Sin[omegadrive * time], 500];
magnSPM[H_, m_] = Coth[1/(kB T) m μ0 * H] - (kB T) / (m μ0 * H);
magnmoment[saturationmagnetization_, diameter_] =
  saturationmagnetization * ((diameter * 10^(-9)) / 2)^3 * Pi * 4 / 3;
```

Careful setup of sampling parameters for DFT

In[418]:=
```
fdrive = 25 000;
omegadrive = 2 * π * fdrive;
fsample = fdrive * 100;
periods = 1;
length = periods / fdrive;
deltat = 1 / fsample;
deltaf = fsample / samplepoints;
tvec = Table[time, {time, 0, length - deltat, deltat}];
samplepoints = Length[tvec];
Bdrivesamples = Map[Bdrive, tvec];
```

Build frequency vectors: absolute and normalized

In[428]:=
```
freqvec = Table[freq, {freq, 0, fsample - deltaf, deltaf}];
freqvecnorm = freqvec / fdrive;
```

Build diameter list

In[430]:=
```
mindiameter = 5 / 2; (* [nm] *)
maxdiameter = 50;
diametersteps = 95;
diameters = Table[dia,
   {dia, mindiameter, maxdiameter, (maxdiameter - mindiameter) / (diametersteps - 1)}];
```

For each diameter:

- sample signal
- build correctly normalized DFT with 200 digit precision
- extract odd harmonic's amplitudes

In[434]:=
```
normFFTtimeDerivative[samples_, freqvec_] :=
 Module[{data = samples, freqs = freqvec, fft},
  fft = Chop[2 * Abs[i * 2 * π * freqs * Fourier[
          N[data, 200], FourierParameters → {1, -1}
        ]] / samplepoints, 10^-190];
  fft[[1]] = fft[[1]] / 2;
  fft
 ]
magnSamples[BdriveSamples_, diameter_, M0_] :=
 Module[{Bsamples = BdriveSamples, d = diameter, satmag = M0, samples},
  samples = Table[
    Quiet[magnSPM[Bsamplepoint / μ0, magnmoment[satmag, d]]],
    {Bsamplepoint, Bsamples}
   ];
  samples[[
     Flatten[Position[samples, Indeterminate]]
    ]] = 0; (* this corrects L(0)=0 *)
  samples
 ]
```

In[436]:=
```
maxharmonic = 13; (* extract harmonic's amplitudes An for n = 3,5,..,13 *)
harmonics = Table[n, {n, 3, maxharmonic, 2}];
harmFreqs = Table[fdrive * h, {h, harmonics}];
harmonicAmplitudesAllDiameters = {}; (* a matrix;
each row gets the amplitudes for one diameter *)
indexOfHarmonic[n_] = fdrive * n * samplepoints / fsample + 1;
Do[
 magnetizationSamples = magnSamples[Bdrivesamples, d, M0];
 spectrumDdtMagnResp = normFFTtimeDerivative[magnetizationSamples, freqvec];
 harmonicAmplitudes = {}; (* gets amplitudes for current diameter *)
 Do[AppendTo[harmonicAmplitudes,
   spectrumDdtMagnResp[[indexOfHarmonic[h]]]], {h, harmonics}];
 AppendTo[harmonicAmplitudesAllDiameters , harmonicAmplitudes];
 , {d, diameters}
]
```

For each diameter:

- **fit amplitude over *n=f/fdrive* exponentially: $A \cdot e^{B-k \cdot n}$**
- **store fit parameters for k-over-diameter-plot**

In[442]:=
```
fitPlots = {};(* List for Plots *)
expFitks = {};(* List for exp fit decay parameter k *)
expFitAs = {};(* List for exp fit parameter A *)
expFitBs = {};(* List for exp fit parameter B *)
expFitRs = {};(* List for exp fit residual R^2 *)
Do[
 data = Transpose[{harmonics, harmonicAmplitudes}];
 (*Print[data];*)
 fit = NonlinearModelFit[data, A * Exp[B - k * n], {A, B, k}, n];
 (*fit=NonlinearModelFit[data,
    A* Exp[B-k*n]+A2*Exp[B2-k2*(n-n0)],{A,A2,B,B2,k,k2,n0},n];*)
 (*fit=NonlinearModelFit[data,A* Exp[B1-(k1*n+k2*n^p)],{A,B1,B2,k1,k2,p},n];*)
 (*Print[fit["BestFitParameters"]];*)
 (*Print[N[fit["RSquared"],35]];*)
 AppendTo[expFitks, k /. N[fit["BestFitParameters"], 5]];
 AppendTo[expFitAs, A /. N[fit["BestFitParameters"], 5]];
 AppendTo[expFitBs, B /. N[fit["BestFitParameters"], 5]];
 AppendTo[expFitRs, N[fit["RSquared"], 25]];
 AppendTo[fitPlots, Show[ListLogPlot[data], LogPlot[fit[f], {f, 0, 25}], Frame → True]]
 , {harmonicAmplitudes, harmonicAmplitudesAllDiameters }
]
(* display fitPlots and result: plotdataExpDecay=Transpose[{diameters,expFitks}];
ListPlot[plotdataExpDecay] *)
```

A.3) Fit SPM to MMF2: Find effective magnetic core diameter corresponding to high local concentration

---

Define constants and magnetization functions

In[13]:=
```
Clear[Evaluate[Context[] <> "*"]]
μ0 = 4 * Pi * 10^(-7);
kB = 1.3806504 * 10^(-23);
T = 300;
magnmoment[saturationmagn_, diameter_] =
  saturationmagn * ((diameter * 10^(-9)) / 2)^3 * Pi * 4 / 3;
magnetitemolvolm3 = 0.0000445254999688228;
cliter[ρnorm_] = 1 / 1000 * ρnorm / magnetitemolvolm3;
ρnorm[cliter_] = 1000 * cliter * magnetitemolvolm3;
relmagnMMF2[H_, ρnormiert_, m_, M0_] =
```

$$\text{Coth}\left[\frac{1}{kB\,T}\,m\,\mu 0\left(H+\frac{1}{3}\,M0\,\rho\text{normiert}\left(-\frac{kB\,T}{H\,m\,\mu 0}+\text{Coth}\left[\frac{H\,m\,\mu 0}{kB\,T}\right]\right)\left(1+\frac{1}{48}\,M0\,\rho\text{normiert}\left(\frac{kB\,T}{H^2\,m\,\mu 0}-\frac{m\,\mu 0\,\text{Csch}\left[\frac{H\,m\,\mu 0}{kB\,T}\right]^2}{kB\,T}\right)\right)\right)\right]-(kB\,T)\Big/\left(m\,\mu 0\left(H+\frac{1}{3}\,M0\,\rho\text{normiert}\left(-\frac{kB\,T}{H\,m\,\mu 0}+\text{Coth}\left[\frac{H\,m\,\mu 0}{kB\,T}\right]\right)\left(1+\frac{1}{48}\,M0\,\rho\text{normiert}\left(\frac{kB\,T}{H^2\,m\,\mu 0}-\frac{m\,\mu 0\,\text{Csch}\left[\frac{H\,m\,\mu 0}{kB\,T}\right]^2}{kB\,T}\right)\right)\right)\right)$$

```
relmagnSPM[H_, m_, M0_] = Coth[H m μ0 / kB T] - kB T / H m μ0;
relmagnMMF2d[H_, ρnormiert_, d_, M0_] =
  relmagnMMF2[H, ρnormiert, magnmoment[M0, d], M0];
relmagnSPMd[H_, d_, M0_] = relmagnSPM[H, magnmoment[M0, d], M0];
```

Prescribe real particle properties and magnetic field cut-out

In[25]:=
```
Bmin = 0; (* define cut-out for fitting functions *)
Bmax = 0.02;
Hmin = Bmin / μ0;
Hmax = Bmax / μ0;
satmag = 480 000; (* Magnetite *)
FeConc = 12;(* real local particle density in mol/l Fe *)
dens = ρnorm[FeConc / 3]; (* iron concentration → normed density *)
realdiameter = 15; (* real particle diameter *)
```

Investigate difference between SPM and MMF2: integrate over squared difference

In[33]:=
```
(* Sum up quadratic difference between functions within magnetic field cut-out *)
quaddiff[effectivediameter_] := NIntegrate[
  (relmagnMMF2d[H, dens, realdiameter, satmag] -
     relmagnSPMd[H, effectivediameter, satmag])^2,
  {H, Hmin, Hmax}]
quaddiff[realdiameter]
```

Out[34]= 1291.28

Fit SPM to MMF2 curve with an effective diameter

In[35]:=
```
minimization = Quiet[NMinimize[{quaddiff[deff], realdiameter < deff < 50}, {deff}]]
effectivediameter = deff /. minimization[[2]];
```

Out[35]= {7.5991, {deff → 22.7003}}

In[38]:=
```
Plot[{relmagnMMF2d[H, dens, realdiameter, satmag],
   relmagnSPMd[H, realdiameter, satmag], relmagnSPMd[H, effectivediameter, satmag]},
  {H, Hmin, Hmax}, PlotRange → {0, 1},
  LabelStyle → Directive[Bold, 14], Frame → True, Ticks → False,
  PlotStyle → {Directive[Thick, Black],
    Directive[Black, Dashed], Directive[Black, Thick, DotDashed]},
  FrameLabel → {Style["H  [A/m]", 19], Style[M_rel, 19]} , RotateLabel → False,
  ImageSize → {500}];
```

Appendix B: Matlab source codes

```
% Appendix B.1
function mmf2_magn_norm = mmf2_magn_norm(H_norm, m, normed_density, satmagn, T)
    % Relative magnetization of a ferrofluid:
    % Implementation of second order modified mean-field theory (MMF2) [1]
    % by Jan-Philip Gehrcke (jgehrcke@gmail.com) -- Universität Würzburg
    %
    % MMF2 is based on Langevin's single particle model,
    % but uses an effective field H_eff:
    % RelMagnMMF2(H,normed_density) = L(a)
    % with L(a) = coth(a) - 1/(a) and a = (mu0 m H_eff)/(kB T)
    % H_eff is a big term. It depends on H and the normed_density.
    %
    % params:
    %       m:              magnetic moment of a single particle [Am^2]
    %       T:              temperature [K]
    %       H_norm:         a vector/list of magnetic field values [A/m]
    %       normed_density: normed density of particles [0,1]
    %       satmagn:        particle's bulk material's saturation
    %                       magnetization [A/m]
    %
    % [1] AO. Ivanov and OB. Kuznetsova. "Magnetic properties of dense
    %     ferrofluids: An influence of interparticle correlations".
    %     In: Phys.Rev. E 64 (2001), p. 041405.

    % Define constants:
    mu_0 = 4 * pi * 10^(-7);   % magnetic field constant [Vs/(Am)]
    kB = 1.3806504 * 10^(-23); % boltzmann constant [J/K]

    % Now calc MMF2 response for each H value given.
    % These terms are needed multiple times:
    m_mu_0 = m * mu_0;
    kB_T = kB * T;
    satmagn_dens = satmagn * normed_density;
    H_norm_m_mu_0 = H_norm .* m_mu_0;
    H_norm_m_mu_0_kB_T = H_norm_m_mu_0 ./ kB_T;

    % This big term is needed two times:
    blubb0r = m_mu_0 .* ...
    (H_norm + ...
        (satmagn_dens .* ...
            (-(kB_T ./ H_norm_m_mu_0) + coth(H_norm_m_mu_0_kB_T)) .* ...
            (1 + (satmagn_dens .* (kB_T ./ (H_norm .^ 2 .* m_mu_0) - ...
                (m_mu_0 .* csch(H_norm_m_mu_0_kB_T) .^ 2) ./ kB_T)) ./ 48 ...
            ) ...
        ) ./ 3 ...
    );

    % Langevin function
    mmf2_magn_norm = coth(blubb0r ./ kB_T) - kB_T ./ blubb0r;

    % A zero in the input leads to "not a number" (NaN) in the output,
    % due to coth(0)-1/0. Analytically, this term is known to be zero.
    % So, find the NaNs and replace them with zeros:
    mmf2_magn_norm(isnan(mmf2_magn_norm)) = 0;
```

```
% Appendix B.2

% This is an optimized implementation of vector field calculations
% for MPS/MPI. The nth higher harmonic's amplitude is calculated for many
% different excitation field / offset field combinations. Both are
% considered and treated as vectors. The (relative) magnetization response
% is calculated in terms of the SPM. The code presented is only the core of
% data _creation_, data usage and evaluation is not shown, as well as a
% huge header of variable definitions.

% by Jan-Philip Gehrcke (jgehrcke@gmail.com) -- Universität Würzburg

% at this point, many variables already have to be initialized:
%    - physical constants, ..., particle material&diameter
%    - the sampling constants for DFT and its interpretation
%    - the magnetic field parameters, as e.g. `B_exc_abs_start`

% *** loop over B_exc
for B_exc_abs = linspace(B_exc_abs_start,B_exc_abs_end,B_exc_abs_steps)
    B_exc = [0;0;1] * B_exc_abs; % excitation field amplitude in z-direction
    H_exc = B_exc / mu_0;
    % *** loop over B_off
    for B_off_abs = linspace(B_off_abs_start,B_off_abs_end,B_off_abs_steps)
        B_off = [0;1;0] * B_off_abs; % offset field in y-direction
        H_off = B_off / mu_0;
        % *** build total field over time (via vector addition)
        % ************************************************************************
        H_in = bsxfun(@plus,H_off,H_exc*sin(omega_in * t_vec));
        % build norms of field: [norm(H(t)), norm(H(t+dt))]
        H_in_norms = sqrt(sum(H_in.*H_in));
        % *** build relative magnetization response as given by SPM
        % ************************************************************************
        mu0mH = mu_0 * m *H_in_norms;
        spm_rel_mag = coth(mu0mH/kBT) - kBT./mu0mH;
        % A zero in the input leads to "not a number" (NaN) in the output,
        % due to coth(0)-1/0. Analytically, this term is known to be zero.
        spm_rel_mag(isnan(spm_rel_mag)) = 0;
        % build M_rel_vec = L(|H|) * unitiyvec(H)
        % build the unityvectors of H(t)
        H_in_vec_unity = bsxfun(@rdivide,H_in,H_in_norms);
        H_in_vec_unity(isnan(H_in_vec_unity)) = 0;
        % build M_rel_vec by multiplying absolute value with direction
        M_rel_vec = bsxfun(@times,spm_rel_mag,H_in_vec_unity);
        % *** acquisition by inductivity and Fourier analysis of M's time
        % *** derivative: DFT of M and multiplication with i omega
        % ************************************************************************
        fft_M = fft(M_rel_vec(3,:)); % acquire and evaluate 3rd z component
        spectrum_dt_M  = 2 * abs(1i*2*pi*realfreqs.*fft_M) / samplepoints;
        % *** extract A_n information for current B_exc / B_off combination
        % ************************************************************************
        harmonic = 3;
        indexofharmonic = f_in*harmonic*samplepoints/f_sample + 1;
        ampl = spectrum_dt_M(indexofharmonic);
    end
end
```